A Case Study of Debris Characterization by Remote Sensing

R. Sridharan
W.I. Beavers
E.M. Gaposchkin
R.L. Lambour
J.E. Kansky

18 December 1998

Lincoln Laboratory

MASSACHUSETTS INSTITUTE OF TECHNOLOGY

LEXINGTON, MASSACHUSETTS

19990119 103

The ESC Public Affairs Office has reviewed this report, and it is releasable to the National Technical Information Service, where it will be available to the general public, including foreign nationals.

FOR THE COMMANDER

Gary Tutungian
Administrative Contracting Officer
Contracted Support Management

MASSACHUSETTS INSTITUTE OF TECHNOLOGY
LINCOLN LABORATORY

A CASE STUDY OF DEBRIS CHARACTERIZATION
BY REMOTE SENSING

R. SRIDHARAN
W.I. BEAVERS
E.M. GAPOSCHKIN
R.L. LAMBOUR
Group 91

J.E. KANSKY
Group 94

TECHNICAL REPORT 1045

18 DECEMBER 1998

LEXINGTON   DTIC QUALITY INSPECTED 3   MASSACHUSETTS

TABLE OF CONTENTS

LIST OF FIGURES

LIST OF TABLES

1. INTRODUCTION

There has been substantial concern on the part of NASA, induced by the growing level of man-made debris in orbit, regarding the long-term safety of human beings on board the space station Freedom. The causes of the concern were two-fold: the debris count exceeds the natural meteorite count by a substantial margin at the larger sizes (>0.1 cm) and there is a large uncertainty in the debris count and density. The typical velocity of impact is ~10 km/s and hence even small centimeter-sized debris can cause catastrophic damage. Several actions were taken by NASA to address the concern:

1.) A modeling effort was initiated to extend the debris count and density distribution from the known catalog (larger than 0.5 meter) to smaller sizes.

2.) A measurement program was started using optical sensors and radars to lend credence to the models.

3.) A protection strategy was designed into the space station to alleviate damage due to impacts by orbiting objects smaller than 1 cm. characteristic dimension.

These initiatives have been quite successful in quantifying the risk and in addressing mitigation strategies. The debris model has been revised and corrected using data from actual impacts on the shuttle, the LDEF and, for the most significant threat sizes of ~5 mm. to 5 cm., from the Haystack radar (Ref. 1,2). The recent report (1) from NASA/JSC indeed indicates that extensive measurements with the Haystack radar show a debris density that is approximately 5 times *lower* than the original models indicated at the altitudes of concern to the space station. However, Haystack measurements have shown that the debris density in some orbits is much higher than originally believed.

1.1 ANOMALOUS DEBRIS AND THE HAYSTACK RADAR

Figure 1 gives the pertinent characteristics of the Haystack radar. The radar is operated in a "stare" mode for debris data collection, *ie.,* the radar is pointed at an azimuth and elevation over a slant range extent. The earth's rotation creates a scan of space. Data are recorded whenever a preset threshold of detection S/N ratio is exceeded. These data are processed by NASA/JSC and result in cumulative statistics of detection as well as orbit and size characterization. One method of presenting the results is shown in Figure 2, which is taken from Ref. 2. This figure represents the rate of detections in the Haystack beam when pointed at zenith as a function of the altitude of detection. The lower curve is a simulation of the detection rate for the known catalog carried by SSC while the upper curve is the detection rate obtained from the Haystack data. NASA/JSC estimates that the total rate across all altitudes sampled (< 1500 km) is ~6.25 objects/hour.

1
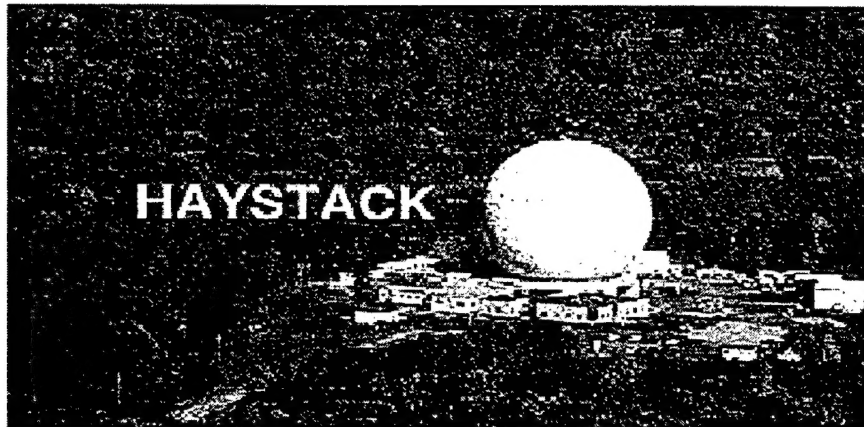
Figure 1. Haystack Radar [10 GHz. X-Band Radar, 36 M. Antenna, IFOV 1 mrad, S/N ratio of 58dB on a 1 sq. m. target at a range of 1000 Km.]
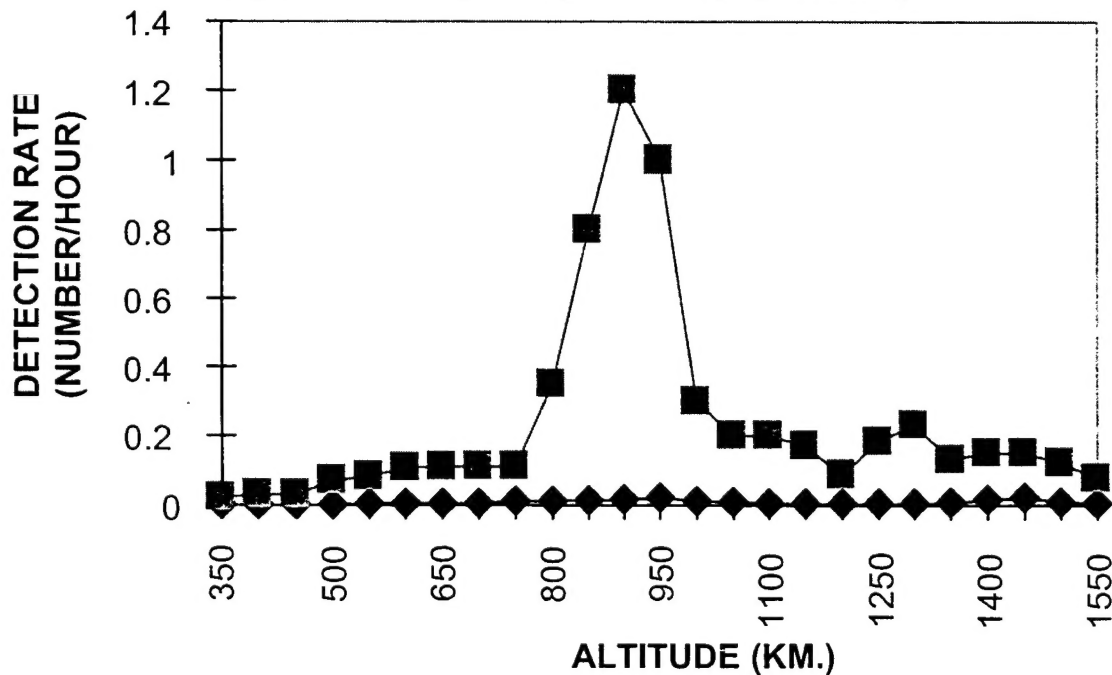
Figure 2. Debris Detection Rate from Haystack

Most of the debris detections shown in Fig. 2 are concentrated in the altitude range between 800 km and 1000 km though there is a noticeable but smaller peak in rate of detection around 1400 km. The subject of this report is the debris in the region between 800 km and 1000 km. NASA/JSC has analyzed these detections extensively and concluded that (Ref. 3):

1.) the debris density exceed that predicted by the original model by a substantial factor;

2.) the debris are primarily small (< 2 cm. size) and largely spherical in shape;

3.) the debris are concentrated in orbits of inclination ~65° and altitudes of 900 - 1000 km;

4.) the debris are primarily in circular orbits;

5.) the debris are likely to be leaked sodium-potassium (NaK) coolant from the Bouk class of nuclear power sources of a Soviet satellite system, called ROR-SAT (Ref. 4), which were put into this type of orbit for long-term storage to allow their radioactivity to decay;

6.) there are 50000-70000 such debris > 8 mm. in size at these altitudes and that these constitute approximately half the total debris population below 1500 km altitude.

This band of debris is termed "anomalous debris" in this report because the debris density exceeds theoretical models by a significant factor.

1.2 SCOPE OF THE REPORT

Remote sensing of small debris in space is a challenging task because of the low signal-to-noise (S/N) ratios that can be attained by ground-based sensors for detection and tracking. However, characterization of space debris is important, as it is one of the factors affecting the short-term and long-term safety of humans in space and of orbiting space-craft. In this report, we present techniques developed at MIT Lincoln Laboratory for re-mote sensing and characterization of a particular debris field and discuss the results. High power radars and high sensitivity optical systems were used for this effort because of their unique and complementary capabilities. Following the data analysis, a theoretical modeling effort was undertaken to infer additional properties of the debris

NASA/JSC funded an effort at Lincoln Laboratory to detect, track and character-ize a sample set of debris in the anomalous debris band. While NASA's analysis used detection data of large numbers of debris in this band, we attempted to characterize in detail a small number of representative samples from this band using the radar and optical sensors operated by M.I.T. Lincoln Laboratory. These sensors are located at Westford, MA, Kwajalein Atoll, Marshall Islands and White Sands Missile Base, New Mexico. The major purpose was to provide evidence supporting or contradicting the conclusions ar-rived at by NASA/JSC. In particular, our characterization involved the following steps:

1. Establish orbits on sample set of debris from this band.
2. Determine the shape and size of the debris using radar data.
3. Assess the surface characteristics of the debris using visible wavelength opti-cal data.
4. Compute the mass and density of the tracked debris.
5. Assess the state (solid/liquid) of the tracked debris.

The primary conclusion from this work is that the properties of the debris sample tracked *are consistent with the hypothesis that they are NaK coolant, and that they are likely to*

be in the liquid state. The rest of this report will describe the techniques used and the results obtained to support this conclusion.

2. DEBRIS DETECTION

Three different strategies were used for the detection and acquisition of debris for characterization. These were:

1. Search in orbit of putative parent satellites
2. Stare and Chase using optical systems and radars
3. Search in the orbits of debris found.

2.1. ORBIT SEARCH OF PUTATIVE PARENTS

The radar cross-section for a 2 cm diameter sphere at L-band (1295 MHz.) is –49 dBsm. and at X-band (10 GHz.) is –35 dBsm. A quick assessment of the sensitivity of the Millstone hill radar (see Figure 3 for radar parameters) indicated that a new search mode was needed for the search. Historically the radar searches along the orbit of a satellite with known orbital elements. However, for the small objects considered here, it was better to search at a relatively low range at an elevation of approximately 30°; *ie.*, search along the orbit by staring at approximately the same range and the same elevation in the orbit of an object while letting time pass. Both the Haystack and the Millstone Hill radars modified their software to construct this search mode.
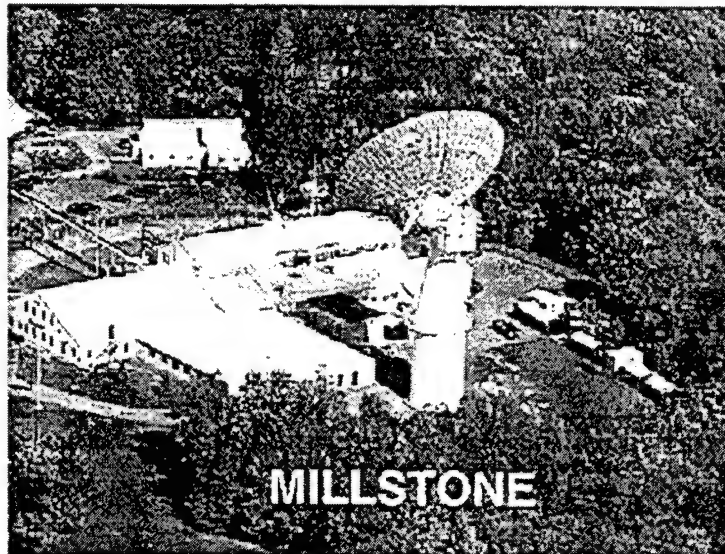
Figure 3. Millstone Hill Radar L-Band, 1, 3 GHz., 25 m. Antenna, IFOV 8 mrad, S/N ratio of 50 dB on 1 sq. m. target at 1000 Km.

The Millstone Hill radar searched the orbits of ten putative parents (out of a total of less than twenty) using the new search mode. The search was always centered about the location of the parent to ensure that the parent was detected and thus validate the parameters of the search. The search mode was capable of detecting a 2 cm. diameter object in orbit with coherent integration[1] and approximately a 3.5 cm. size object in orbit with non-coherent processing. No detection resulted.

If there were any recent slow leaks of debris of the size postulated, the difference in rate of change of the right ascension of the ascending node between the "parent" and the "child" orbits would have been small (<0.01 deg./day). As a result, the "child" would have been found by Millstone in the search. *Hence it can be positively stated that none of the parent objects whose orbits were searched had recently (within 30 days of the search) leaked any debris of size >=2 cm.*

2.2. STARE AND CHASE - OPTICS AND RADARS

The Experimental Test System located in New Mexico (Figure 4) is a visible wavelength optical system that was a proof of concept for the GEODSS. It has two 30 in. telescopes each with a diagonal FOV of > 20 mrad. The system uses a Vidicon camera and has a detection sensitivity of ~15.5 V_M. The ETS conducted several stare-and-chase sessions for debris under Air Force sponsorship in 1994. The system is capable of detecting a resident space object, correlating it against the catalog and, if uncorrelated, transitioning from stare to tracking the object essentially in near real time (Ref. 5). ETS found one piece of anomalous debris that has been characterized extensively.
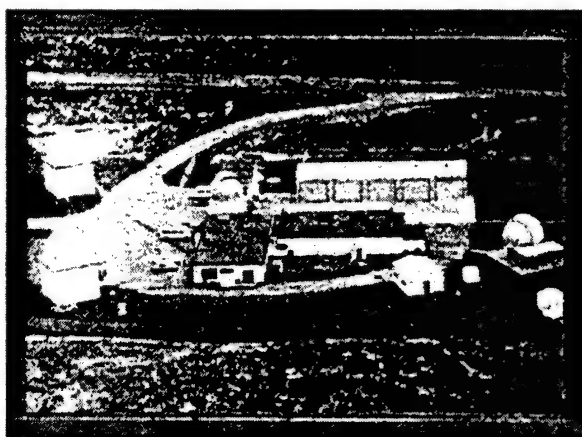
0.75 m. Telescopes with CCD Camera, IFOV 1 ⁰ or 2⁰
Detection Sensitivity ~15 - 17 m $_v$
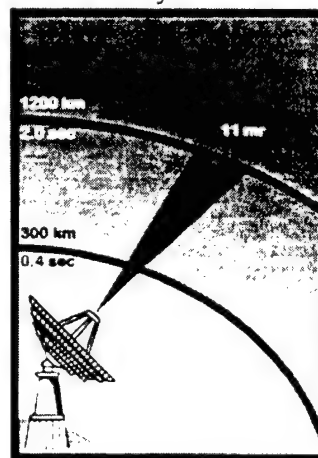
L-Band, 1320 MHz., IFOV 8 mrad,
48 dB S/N ratio on 1 sq.m. target at 1000 Km.

Figure 4. ETS at White Sands Missile Base on left, TRADEX at Kwajalein on right.

---

[1] The Millstone hill radar processes M*2^N (M < 10, N ≤ 9) radar pulse returns together accounting for target movement during the integration interval. Were a target stable in attitude, the returns would add "coherently" yielding a combined S/N ratio of 2^N times that from a single pulse. If the target is tumbling, the returns would add "non-coherently" with a total S/N ratio of 2$^{N/2}$ times that from a single pulse.

TRADEX is an L-band radar located on the Kwajalein atoll in the Marshall islands (Figure 4). TRADEX conducted several stare and chase sessions during 1995 under NASA/JSC sponsorship. The operating principle for TRADEX is the same as for ETS. The radar points at a specific azimuth and a specific high elevation and examines a range between 500 and 1200 km. The radar's sensitivity is such that it should detect any object > 3.5 cm in diameter in this altitude range. TRADEX detected one known and one uncorrelated RSO per hour on an average (Ref. 6). The radar found four anomalous debris during its operations.

2.3 SEARCH OF ANOMALOUS DEBRIS ORBIT PLANES

If the anomalous debris were a result of the leaking of a liquid, it seemed likely that there would be many "droplets" per orbit plane. Hence the orbit planes of some of the debris found by ETS and TRADEX were extensively searched with the Millstone Hill radar. The sensitivity of Millstone is such that it should detect any metallic sphere > 2 cm. in diameter in the search. Millstone found 6 more anomalous debris.

Finally, some of the debris orbits were searched with the Haystack radar. Haystack is the most sensitive of the radars used in this effort. It should detect debris of size > 1 cm. Haystack found 8 more debris objects though, unlike the eleven above, these were not completely characterized.

2.4. RESULTS OF SEARCHES FOR ANOMALOUS DEBRIS

The purpose of this project was to characterize a sample set of anomalous debris, which required finding and tracking them regularly. A special search mode was developed for the radars. The efficacy of the stare and chase algorithms at the radars was demonstrated. Eleven debris objects were found and extensively characterized. Eight more debris objects were found but were incompletely characterized.

A key finding of the search is that there are multiple debris objects per orbit plane. This implies a common parentage and time of origin for the debris, which is consistent with a leaking liquid.

3. RADAR DATA ANALYSIS

Extensive data were collected with the Millstone and Haystack radars on the eleven debris objects found during the search. The objectives of the data collection were the following:

1. Signature data (radar cross-section vs. time) to assess spin period, any temporal variability and also to estimate size.
2. Polarization data (the ratio of the orthogonal polarization RCS to the principal polarization RCS) to assess the shape of the debris.
3. Metric data to support determination of accurate orbits and calculation of the area/mass ratios, mass and density of the debris.

Each of these topics will be discussed below.

3.1 RADAR SIGNATURE AND POLARIZATION DATA

Figure 5 shows representative radar signature data on the anomalous debris as recorded at the Millstone Hill radar. The radar transmits a right circularly polarized signal looking out of the antenna. The principal receive polarization (PP) is consequently left circularly polarized; and the orthogonal receive polarization (OP) is right circular. The radar's tracking program dynamically selects the number of pulses integrated per signal processing cycle based on the S/N ratio required for accurate metric tracking. Typically, the radar operates with a pulse width of 1.04 ms. and a pulse repetition frequency of 40.

Figure 5 shows the temporal history during a track (typically lasting 10 minutes) of the measured PP radar cross-section (RCS) for two of the debris. It is clear that the radar does not detect any temporal structure in the signal at a period longer than the integration interval, which is 1 - 3 seconds. A number of tracks at a variety of aspect angles all exhibit invariant structure of the RCS at a temporal resolution of 1 - 3 seconds. The figure also shows the temporal history of the OP RCS during the same tracks. The apparent structure is actually dominated by noise. It is clear that the OP RCS is below the PP RCS by approximately 25 dBsm. Previous data collection on other typical debris shows that this behavior is quite unusual. Commonly, the OP / PP ratio is of the order of a few dB and varies significantly over the track (Ref. 7, also see Figure 7).

The accumulated statistics of mean PP RCS and the polarization ratio (defined as mean (OP RCS - PP RCS)) for the eleven debris objects are given in Table 1. It is evident that, consistently, the PP RCS is < - 20 dBsm. and the polarization ratio is approximately -25 dB which is close to the isolation between the principal and orthogonal polarization receive channels at the Millstone Hill radar. For comparison, Figure 6 shows a plot of PP and OP RCS of the track of a radar calibration sphere and one of the anomalous debris objects. It is well known that the OP return from spherical objects is negligible compared to the PP return *over all aspect angles for a circularly polarized radar transmission*. Comparison of the sphere RCS signature to those of the debris leads to the conclusion that the debris objects being tracked are spherical in shape. Further, the PP
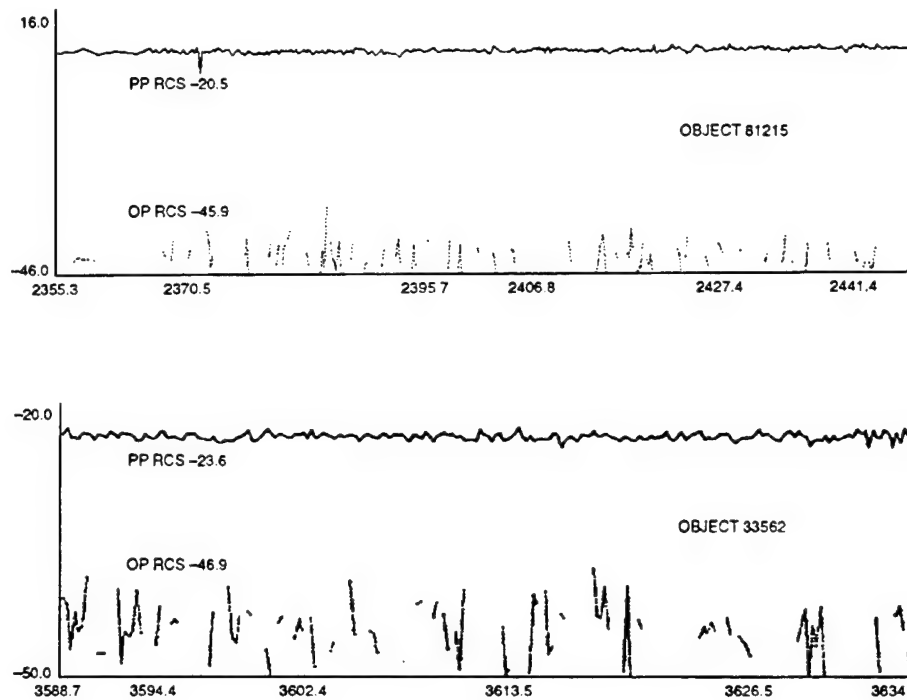
Figure 5. Millstone PP and OP radar cross section data for two anomalous debris pieces: (a) object 81215, (b) object 33562.
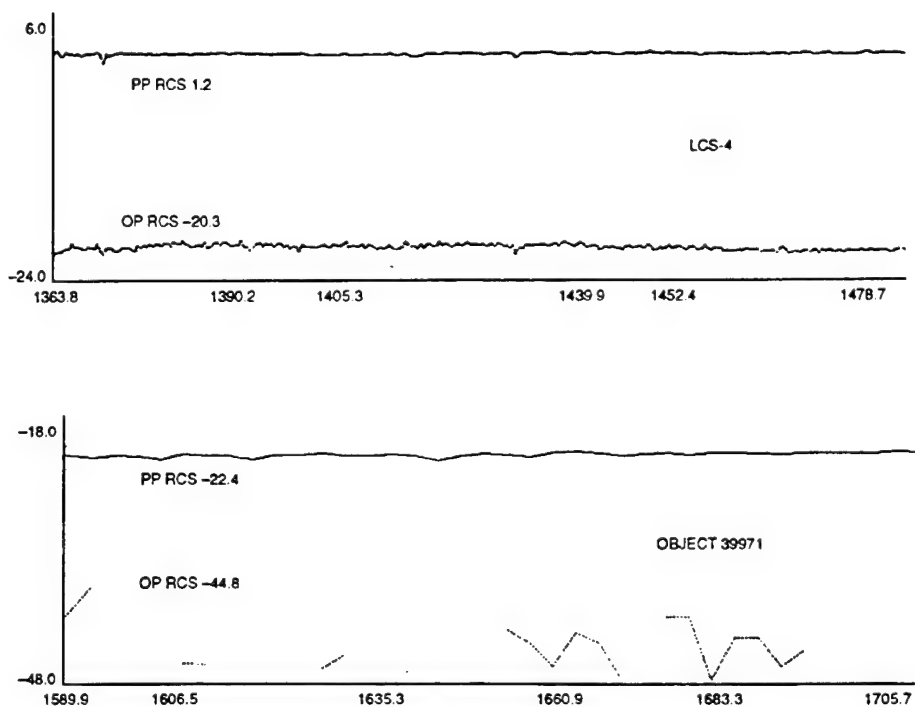
Figure 6. Comparison of Millstone radar signatures for (a) a radar calibration sphere, LCS-4, and (b) one of the anomalous debris objects, 33971.
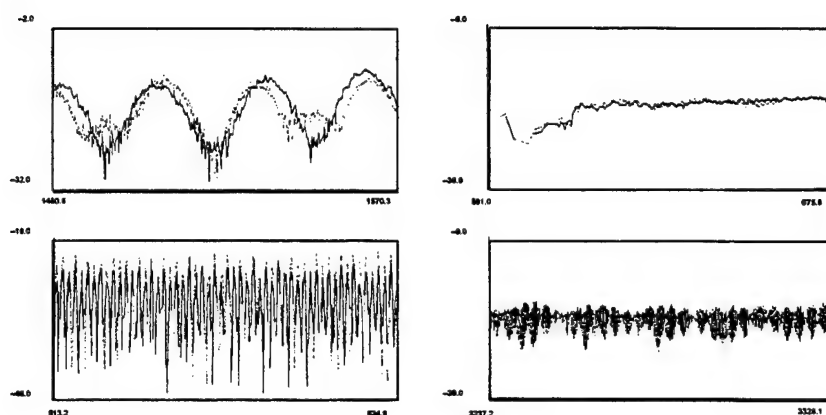
Figure 7. Millstone PP (solid line) and OP (dashed line) radar signatures for four non-anomalous debris pieces. The x-axis displays UT in seconds and the y-axis shows RCS in dBsm.

TABLE 1

Millstone Radar Results

Object Number	<PP RCS> dBsm	Polarization Ratio (dB)	Radius (cm)	Sigma (cm)
81215	-20.8	-24.2	2.84	0.09
33562	-23.6	-21.6	2.55	0.06
33609	-22.4	-23.3	2.68	0.08
33612	-22.1	-25.3	2.71	0.05
33616	-30.7	-25.1	1.94	0.09
39969	-34.3	-21.2	1.70	0.08
39970	-32.3	-25.2	1.83	0.02
39971	-21.9	-24.5	2.73	0.03
39972	-22.1	-24.0	2.70	0.02
39973	-25.4	-21.2	2.38	***

RCS of the debris can be used to infer a radius of the sphere. The results are shown in Table 1 along with the formal uncertainties based on a number of tracks.

A few comments are in order here:

1. The range in radius of the spheres (1.6 cm. to 2.8 cm.) represents at the lower end the detection limit of the Millstone Hill radar and at the upper end perhaps the largest size of the anomalous debris detected so far.

2. The estimated sphere size to radar wavelength ratio for the Millstone hill radar is well in the Rayleigh region. Hence there is little ambiguity in estimating the size from the RCS. Such an ambiguity would arise if the Haystack radar with its 3 cm wavelength were used for the purpose.

3. The formal uncertainties are based on the variability of the estimated mean radar cross-section in the principal polarization channel. No calibration corrections have been applied to these values. It is believed that the RCS estimate at the Millstone Hill radar is good to <1 dBsm generally based on frequent tracks of a large 0 dBsm sphere. The same calibration uncertainty should apply to the small spheres in question because the radar attempts to track all objects at approximately the same S/N ratio (30 - 36 dB). Further, this high S/N ratio is achievable in the case of the small spheres because of the high sensitivity of and the low slant range from the radar.

4. It is assumed that the spheres are perfectly conducting so that the radar theory relating the size to RCS as for example in Ref. 8 applies.

3.2. ESTIMATION OF MATERIAL DENSITY OF DEBRIS

It is well known that the Earth's atmosphere extends beyond the 800-1000 km orbital altitude of the anomalous debris. The atmosphere causes a drag on the debris, which tends to lower their orbital energy and, consequently, the semi-major axis of the orbit. The atmospheric drag force can be represented as:

$$F_d = \tfrac{1}{2}C_d(A / M) \rho v^2 \tag{1}$$

where

F_d = drag force on the debris
C_d = ballistic coefficient
(A / M) = the ratio of the projected surface area to the mass of the debris
ρ = the density of the atmosphere at the debris altitude
v = the velocity of the debris relative to the atmosphere

Hence, with accurate metric data over many orbits, it is feasible to estimate an average area/mass ratio for the debris found in this project. Given that the debris objects are spherical, there is no dependence of the area/mass ratio on aspect angle. The area and volume can be calculated from the size reported in Table 1. Hence the mass and density can be computed.

The caveat in the chain of logic in the last paragraph is that the atmospheric density model at the altitudes of these anomalous debris is subject to considerable (~15-30%) uncertainty (Ref. 9-11). This problem was addressed by contemporaneous tracking of a well characterized sphere – Lincoln Calibration Sphere #4, SCC object no. 5398 – which happens to be in an orbit of similar altitude. Since all of the relevant parameters are known for LCS-4, the drag force can be accurately calculated and a scale factor for the atmospheric density could be estimated and used in fitting the metric data on the anomalous debris. The Earth's atmosphere is assumed to be corotating, so that v is known, and C_d is assumed to be that for a sphere (~2.2); this allows computation of (A/M) and the density follows.

The metric data used came largely from the Millstone Hill radar whose calibration is maintained extremely well. The quality of the data is shown in Table 2. The results of the procedure detailed above are shown in Table 3. It is evident that the "mean" density of the spheres is just over 1 gm/cc, which is similar to that of water.

TABLE 2

Millstone Hill Radar Performance

Parameter	Accuracy
Radar Cross section	1 dBsm.
Range	5 meters
Range Rate	10 mm/sec.
Angles	5 mdeg. (0.1 mrad.)

TABLE 3

Anomalous Debris Mass and Density Estimates from MHR Data

Object Number	A/M (cm^2/gm)	N	Mass (gm)	Density (gm/cm^3)
81215	0.253±0.007	31	100.2±9.1	1.044±0.06
33562	0.273±0.066	6	74.8±9.6	1.077±0.11
33609	0.225±0.011	7	100.2±10.8	1.244±0.10
33612	0.256±0.006	5	90.1±5.4	1.031±0.04
33616	0.349±0.009	6	33.8±4.0	1.108±0.08
39969	0.464±0.22	3	19.6±3.0	0.953±0.09
39970	0.545±0.043	2	19.3±2.1	0.752±0.07
39971	0.247	1	94.8	1.112
39972	0.307	1	74.6	0.905

Reference 4 indicated that eutectic NaK was probably used as the coolant in the nuclear power sources used on the Soviet satellites that are suspected to be the parents of these debris. Figure 8 gives the variation of density of eutectic NaK with temperature drawn from Ref. 12. It is clear that the density of eutectic NaK at ~300 °K is 0.9 gm/cc. similar to the density of the anomalous debris given in Table 3.

$$\rho = 940.598 - 0.241 * T$$
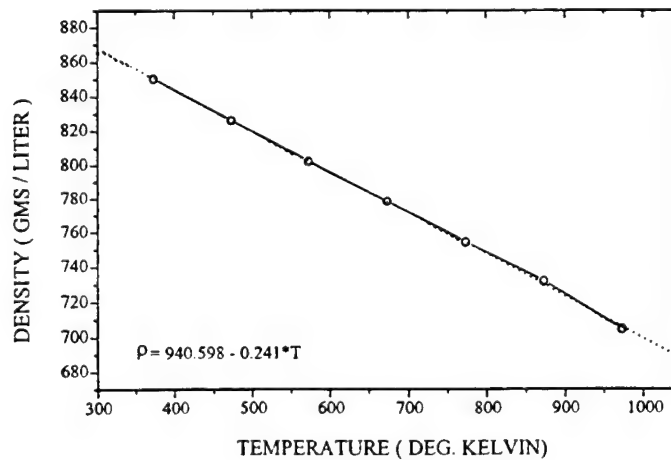
Figure 8. Density of eutectic NaK alloy as a function of temperature.

3.3. SUMMARY OF RESULTS FROM RADAR DATA ANALYSIS

The following conclusions have been reached as a result of collection and analysis of signature, polarization and metric data from the radars.

1. *The debris found and tracked exhibit without exception a polarization ratio at all aspect angles indicative of a spherical shape.*
2. *The debris found and tracked exhibit radii varying between 1.6 cm. and 2.8 cm.*
3. *The spheres have a mean density of ~1 gm./cc. consistent with eutectic NaK at typical orbital temperatures.*

4. OPTICAL CHARACTERIZATION OF THE DEBRIS

Optical telescopes with appropriate instrumentation may also be used to determine some of the physical properties of the orbital debris objects. The gradual change of the sun-debris-sensor angular relationship (phase angle) during any given orbital pass provides an opportunity to explore a robust variety of configurations for the debris solar reflections. High precision optical photometric and polarimetric measurements during such passes produce photometric and polarimetric "phase curves". Subsequent analyses of these phase curves may, under favorable circumstances, provide the means to obtain estimates of object size and to determine its relative metallic or dielectric nature.

4.1 INSTRUMENTS AND PROCEDURES

The requirement of keeping the optical image of the orbiting debris object on the same subset of detector pixels during the 10 to 20 second exposures needed to secure sufficient counts for a high precision optical measurement is quite stressing. Furthermore, when attempting such measurements with a single sensitive CCD, it implies that the field of view (FOV) with enough sensitivity for detecting and measuring the debris objects will be small. In the present study the MIT Firepond Optical Facility 1.2 m telescope with 1 mrad FOV has been employed for all photometric and polarimetric measurements. This tracking telescope system is capable of holding the rapidly moving near-earth debris objects at a fixed position on the instrument focal plane CCD detector during the exposures. The debris objects are sufficiently faint, however, that they are generally not easily visible in the less sensitive wide field finders.

Since it is important to obtain as many high quality measurements as possible during any given object pass, rapid acquisition is essential. However, the small sensor FOV, and the low sensitivity of the wide field finder telescope make this difficult. Furthermore, the orbital element sets for the debris are usually not of sufficient quality to permit blind pointing of the optical telescope/sensor system for objects in low orbits. It is here that one of the most important aspects of the Firepond telescope facility comes into play (Figure 9). The real-time link between the telescope and the Millstone and Haystack radars allow the radars to hand off pointing for the telescope. By this means it is often possible to get the telescope pointed and tracking properly even while the debris may be in Earth's shadow or to begin the collection of optical measurements near the beginning of a pass while the debris object is still at relatively low elevation angles, long before it would be possible by optical means alone. This permits data collection over much greater ranges of phase angles, and this is important in the procedures described in the following sections.
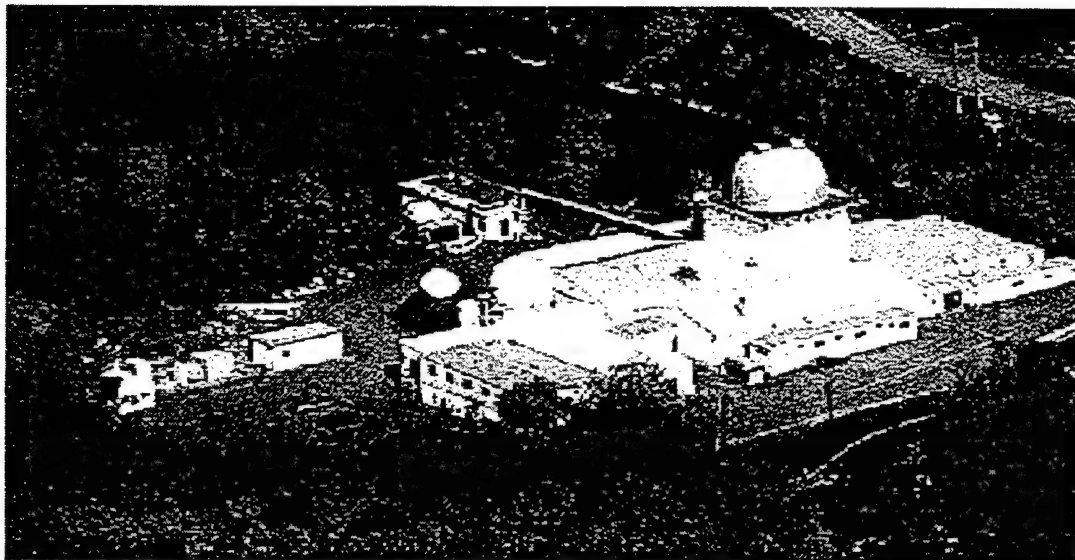
Figure 9. Firepond Optical Facility. 1 meter optics with CCD photo-polarimeter IFOV 1 mrad, ~13 m_v detection sensitivity.

4.2 FIREPOL

The sensor system employed for the optical measurements in this study is FIRE-POL, a combination CCD photometer/polarimeter, i.e., a photopolarimeter. It is basically a chamber containing a CCD mounted at the telescope focal plane. Within this chamber are three elements which are in the optical path in front of the CCD detector. One of these elements is a rotatable wheel which contains a set of glass filters. For this study the V filter of the astronomical UBVRI system was chosen (Ref. 13). The second element is a half-wave plate. The half wave plate is a birefringent material which produces one half wave phase difference between the ordinary and extraordinary wave components (corresponding to the two different refractive indices characterizing such material) passed through it, which emerge orthogonally polarized. The third element is a Savart plate. The two polarizations separate spatially during their passage through the properly oriented Savart plate. The combination of the half-wave plate and the Savart plate thus produces two images on the CCD, one for each polarization. In practice, the sunlight reflected by the orbiting objects will be partially linearly polarized in the plane perpendicular to the plane of incidence containing the sun, observer, and object. By proper rotation of the half-wave plate under real-time PC control during the measurement, the two resulting images will correspond to the polarizations in the plane of incidence (I_2) and perpendicular to that plane (I_1). Thus, the percentage polarization of the reflected sunlight may be determined by the brightnesses (above background) of the two FIREPOL images:

$$\%POL = 100*(I_1 - I_2)/(I_1 + I_2) \qquad (2)$$

while the photometric brightness for that observation may be determined using the total amount of light in each image pair:

$$I = I_1 + I_2 \tag{3}$$

Photometric calibration of the measurements is accomplished by observing a set of selected photometric standard stars at various observed elevations above the horizon during each observing session. These observations over a range of different "air-masses" allows the subsequent determination of the nightly photometric zero point and the nightly extinction coefficient. That information is used for transforming the raw counts in the measured images into "outside the atmosphere" V filter magnitudes. Since each debris object brightness determination is obtained when it is at some variable distance r, it is desirable to convert the measured magnitude to what it would have been at some selected fixed distance. For this study that fixed distance is 1000 km has been chosen, with the corresponding magnitude labeled M1.

Polarimetric calibration is accomplished by observing a selected set of "polarization standard stars". These are stars with previously well determined plane of polarization and %POL. For this purpose a set of measurements of the standard star is made with various orientations of the half-wave plate.

4.3 ANALYSIS PROCEDURE

The combination of simultaneous photometric and polarimetric measurements of the debris may be used to determine high quality estimates of the object size and metallicity as described in the following sections.

4.3.1 Photometry

The predicted brightness (in the V magnitude system) of a solar illuminated object is given by the following equation. (Ref. 14).

$$V = V_{SUN} + 5\log(r) - 2.5\log(\rho\,A\Phi(\phi)) \tag{4}$$

where

V_{SUN}	=	apparent V magnitude of Sun
r	=	distance to object
ρ	=	object albedo (fraction of incident light reflected)
A	=	object cross sectional area
$\Phi(\phi)$	=	phase function for object
ϕ	=	phase angle (angle between sun and observer)

The above equation is simply a statement that the observed light is that fraction ρ of the incident sunlight which is reflected by the area A with some angular distribution $\Phi(\phi)$, and reduced in intensity by the consequences of the inverse square law (i.e. Δmag $= 2.5\log(1/r^2)$).

19

The photometric measurements provide V for the above equation. To deduce A, it is necessary to have values for and $\Phi(\phi)$. The phase angle may be calculated for each measurement based upon the known angular positions of the sun and the object for that time. A sequence of such measurements during any particular orbital pass of the object thus yields a set of magnitude measurements as a function of the phase angle. The role of variable distance to the object is removed by calculating $V - 5\log(r/1000) = M1$. Finally, a plot of M1 versus the phase angle for a set of measurements produces a "photometric phase curve" which shows directly the dependence of Φ on ϕ when A and ρ are constant. Thus, these observed photometric phase curves are the starting point in attempting to interpret and analyze the photometric measurements.

Theoretical phase curves may be calculated for a number of simple object shapes. Of these, the simplest is that of the specularly reflecting sphere, for which the phase function is $\Phi = (4\pi)^{-1}$. This produces a flat photometric phase curve which is constant at all phase angles.

4.3.2 Polarimetry

The final unknown in the determination of A using the previous equation is ρ. The polarization measurements are here employed for this task. At each phase angle the reflected light is assumed to be reflected from the object surface with angles of incidence and reflection equal to half the phase angle ($\Phi/2$). This reflected light will be partially linearly polarized in the plane perpendicular to the sun-object-observer plane by an amount which depends on the optical indices of the surface material. The variation of observed polarization with phase, or "polarization phase curve," will reveal how metallic or dielectric the material is. In practice, the observed polarimetric phase curve is fit by a theoretical expression using the Fresnel equations for reflection. This yields a pair of (n,k) values for the optical indices. In general, since the observed portions of the phase curves generally include measurements between phase angles of ~50 degrees and ~110 degrees, these (n,k) pairs are not unique. However, they do serve the purpose of characterizing the metallicity of the surface, and they also allow a calculation of the normal reflectivity or albedo of the surface using the following expression (Ref.15).

$$\rho = [\,(n-1)^2 + k^2\,] / [\,(n+1)^2 + k^2\,] \qquad (5)$$

It may be shown that although the (n,k) pairs which fit the portion of the phase curve for observations at phase angles less than ~120 degrees are not unique, the ρ values for all such pairs are virtually the same (< 1% scatter). Thus, ρ is an especially useful and appropriate parameter to characterize the polarization phase curves.

4.4 RESULTS

The Firepond debris observations for this study are tabulated in Appendix A as follows:

Column	Entry
1	Day number (for year 1996)
2	UT time of measurement
3	Object identification number
4	Phase angle
5	Range to object in km
6	M1 = V magnitude at 1000km
7	%POL = measured % linear polarization

The measurements in Appendix A have been used to produce the observed phase curves for all the debris objects in Figures 10 and 11. It has been found that some of the polarization measurements at low elevation angles at the beginning or ending of a pass may be anomalously high and show unusual scatter. This is believed to be due to the pollution of the sky background by ground light sources which may be scattered into the beam, often with some residual polarization. The same is true when the object passes near enough to a bright moon where the sky background light pollution confuses the measurement. The most obvious cases of such background problems have been removed from the plots. There are still numerous high excursion data points in both the photometric and polarimetric phase curves. These are expected for such low count rates as the debris objects produce, but do not defeat the analysis since in both the photometry and polarimetry we seek the overall shape and location of the phase curves, and excursions of a few data points generally do not weigh that heavily.
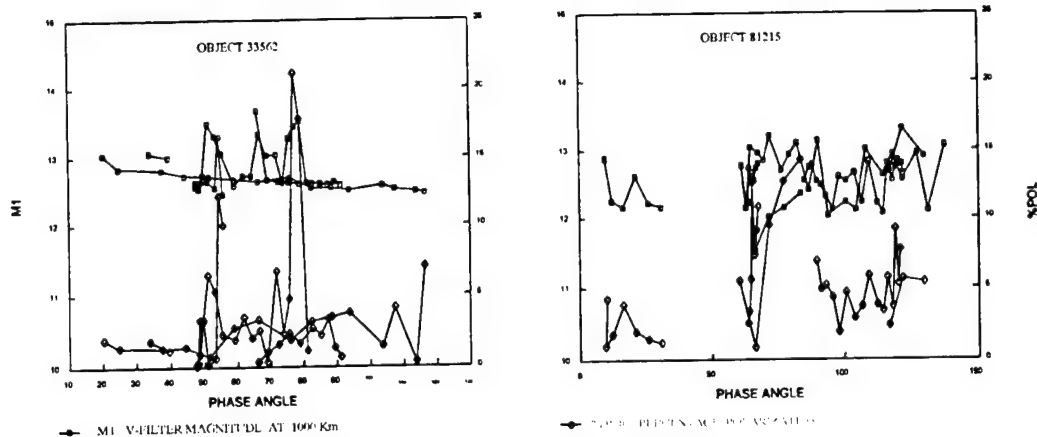
Figure 10. Photometric (M1) and polarimetric (% polarization vs. phase angle) phase curves for two anomalous debris (a) object 33562, and (b) object 81215. The y-axis scale for the photometric (polarimetric) phase curve is on the left (right).
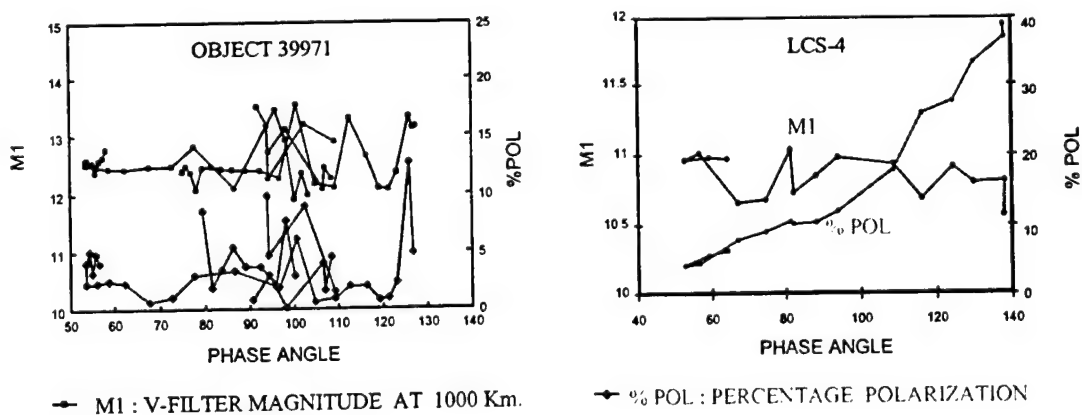
Figure 11. Photometric and polarimetric phase curves for (a) anomalous debris object 39971, (b) specular sphere LCS-4. The format is the same as Figure 10.

The debris data set is remarkably homogeneous compared to any previous study at this site by this instrument. In all cases, the photometric phase curves of these debris objects (after allowing for the inherent noise) do appear to be flat over the entire phase angle range. In each case the flat photometric curve fit appears to be the most reasonable model choice. This allows us to average all the M1 measurements for an object. This value is inserted in the following equation, which is a rewriting equation (4) for the case when $\Phi = (4\pi)^{-1}$, and to solve for the area of the debris object.

$$A_\rho = 12.6\rho^{-1}10^{(3.22 - M1)/2.5} \tag{6}$$

The subscript ρ has been included to emphasize that this is an area value dependent on the polarization measurement and analysis. The results are tabulated in Table 4.

TABLE 4

Summary of Size Estimates from Optical Measurements

Object Number	M1	Reflectivity	Radius (cm)
81215	12.6±0.4	0.89	2.9±0.5
33562	12.8±0.3	0.89	2.6±0.4
33609	12.5±0.2	0.84	3.0±0.3
39969	13.6±0.08	0.89	1.8±0.1
39970	13.5±0.2	0.89	1.8±0.5
39971	12.6±0.4	0.89	2.9±0.5
39972	12.7±0.3	0.84	2.9±0.4

The consistently low polarization for all objects at all phase angles implies that they are all metallic with high reflectivity with only slight differences. The formal error of the M1 values has been propagated to obtain an estimate of the uncertainties of the radii under the assumption that these reflectivity estimates are correct. The radii calculated from the optical measurements are consistent with those calculated from the radar data (Table 1).

5. THEORETICAL ANALYSIS

A low-fidelity thermal model of the anomalous debris using the properties inferred from the radar and optical observations was developed to assess whether the debris are in a liquid or solid state. The conclusion of this model was then applied to a low-fidelity evaporation model to decide whether the orbital lifetimes of the debris are significantly influenced by evaporation.

5.1 TIME-DEPENDENT THERMAL MODEL FOR THE ANOMALOUS DEBRIS

A simple, time-dependent thermal model was constructed which was then used to compute the temperature of the anomalous debris as it orbits the Earth. Using conservation of energy, the rate of change in temperature of a single debris object can be written in the following manner:

$$\frac{dT}{dt} = \frac{(E_{absorbed} - E_{radiated})}{Cm} \tag{7}$$

where the numerator represents the difference between the energy absorbed by the object and the energy radiated by the object, while the denominator represents the product of the specific heat, C, and the mass (also referred to as the thermal mass). Given an initial temperature this differential equation can be solved numerically for the thermal history of the object.

The absorbed energy originates from multiple sources, the most important of which are the sun, Earth-reflected sunlight, and terrestrial long-wave radiation ($E_{absorbed} = E_S + E_{reflec} + E_{therm}$). The absorbed solar energy can be written as:

$$E_S = F_S \alpha A_p \tag{8}$$

where F_S is the incident solar flux (1360 W/m^2), α is the absorptivity, and A_p is the cross-sectional area. The anomalous debris are assumed spherical; therefore, $A_p = \pi r^2$. A grey-body approximation is made for α; *i.e.*, α does not vary with wavelength.

The solar energy input is eliminated when the debris object is in eclipse, which is determined using the following method. Let X be a vector from the sun to the satellite, and P is a vector from the sun to the center of the Earth. The angular radius of the Earth as seen from the sun is:

$$\rho_E = \arcsin\left(\frac{R_E}{P}\right) \tag{9}$$

The satellite will be in eclipse (behind the disk of the Earth) when:

$$\rho_E > \arccos(P \cdot X), \quad \text{and} \quad |X| > |P|. \tag{10}$$

25

This geometry is illustrated in Figure 12.
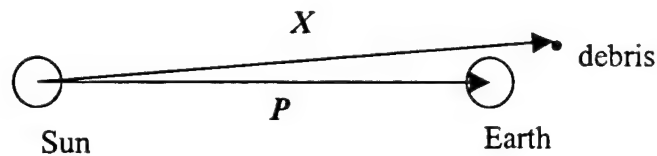
Figure 12. Cartoon of the geometry used to determine whether debris is in eclipse.

Earth-reflected sunlight can be described by an equation of the same form as equation (8). The energy flux of reflected sunlight depends on the altitude of the debris, the albedo of the Earth, and the illuminated surface area of the Earth "visible" to the object. This last quantity is related to the direction cosine of the position vector of the object, the solar position vector, and the altitude the object (Ref. 16, Figure 13). The quantities presented in Figure 3 of Ref. 16 are digitized and used as a "look-up" table to determine the Earth-reflected solar flux. These quantities are reproduced in Figure 14. For example, at 1000 km altitude and a globally-averaged albedo of 0.34, the reflected solar flux is ~450 W/m^2. This look-up table can be scaled to any globally-averaged albedo.
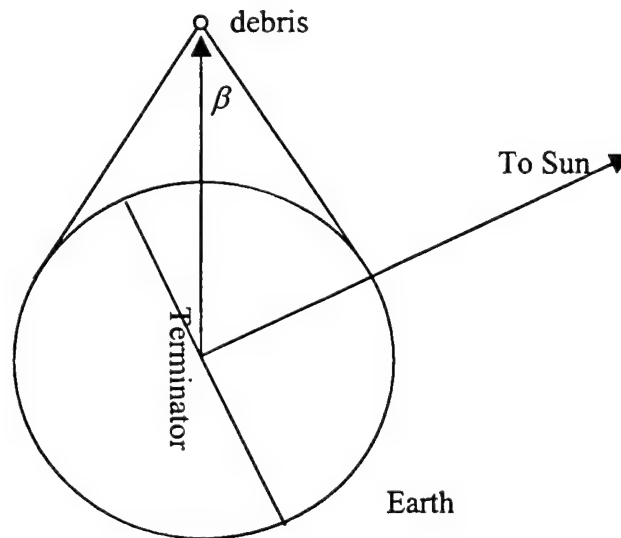
Figure 13. Cartoon depicting the surface area of the Earth visible to a debris object at altitude h and the relation between the debris and solar position vectors. The angle β is defined by equation (13).
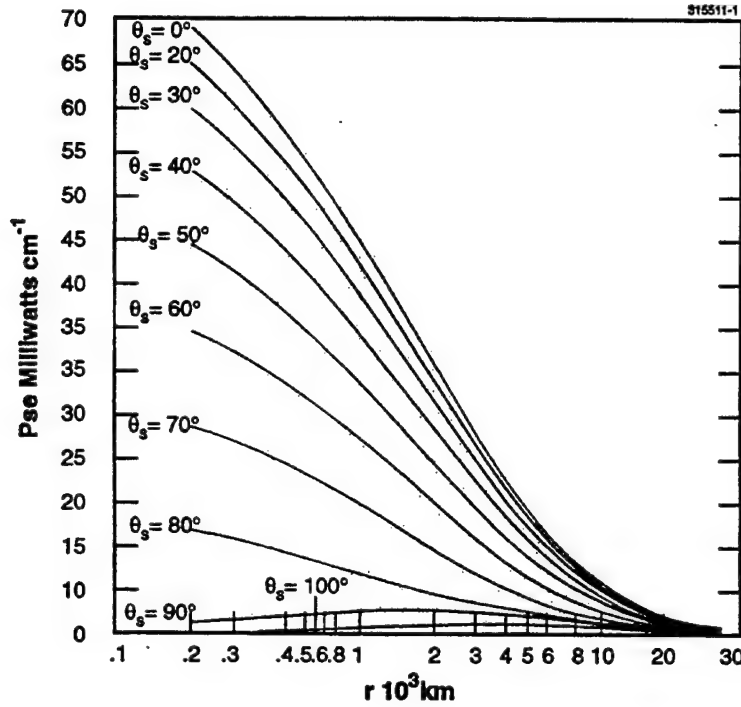
Figure 14. Earth-reflected solar power input per unit cross-sectional area for a spherical satellite as a function of altitude. The angle θ_S is the angle between the debris and solar position vectors. Adapted from Ref. 16.

The terrestrial long-wave radiation input is represented by:

$$E_{therm} = F_{therm}\alpha A_p \tag{11}$$

The thermal energy flux, F_{therm}, is taken to be 238 W/m² at the surface of the Earth, which is a global average and assumes that the Earth is a diffuse radiator (Ref. 17, 18). A black-body approximation is used to determine the radiated energy. Then, the energy radiated to free space can be written as:

$$E_{radiated} = \sigma\varepsilon T^4 A_s \tag{12}$$

where ε is the emissivity, T is temperature, and σ is the Stefan-Boltzmann constant. The surface area, A_s, is taken as $4\pi r^2$. ε is assumed not to vary with wavelength. The radiated energy is affected by the proximity of the warm Earth. This reduces the area of the sphere radiating to free space by a factor of Ωr^2, where $\Omega = 2\pi(1 - \cos(\beta))$. At the altitude of the sphere, h, the Earth subtends a half angle:

27

$$\beta = \sin^{-1}\left(\frac{r}{r+h}\right) \tag{13}$$

The anomalous debris are assumed to consist of eutectic NaK and are spherical in shape. The specific heat and density of eutectic NaK were determined using data from standard engineering tables (Ref. 15,19). The data were plotted and then fit to functions in order to extrapolate the quantities down to the freezing point of eutectic NaK (260.85° K). The specific heat is represented by:

$$C(T) = 1112.19 - 0.608T + 0.000384T^2 \tag{14}$$

and the density is represented by:

$$\rho(T) = 940.6 - 0.241T \tag{15}$$

As the temperature of the droplet varies, these quantities change. The mass of the droplet is assumed to remain constant.

The optical properties of NaK are not well known. Unpublished work by Russian researchers indicates that the absorptivity and emissivity coefficients of the material are believed to be roughly 0.156 and 0.132, respectively. The value for the absorptivity of the material is reasonable because of the radar and optical characterization work reported in the previous sections and the optical work of Russian researchers (Ref. 20, 21). Based on these data it is not likely that debris are transparent; therefore, the reflectivity and absorptivity coefficients should sum to 1.0. The reflectivity values of 0.84-0.89 then lend credibility to the absorptivity value of 0.156. No such "verification" exists for the emissivity value. However, the emissivity values for liquid sodium and liquid potassium are generally low at the temperatures expected on orbit. The total normal emissivity of liquid sodium is on the order of 0.01-0.05 at ~300 °K (Ref. 22, 23). The value for liquid potassium is ~0.01 at ~300 °K (Ref. 24). These values are significantly lower than values reported for NaK (0.132). Nevertheless, it is assumed here that the values α=0.156 and ε=0.132 apply to NaK. The effects of varying them are also discussed below.

To determine the motion of the debris and its effect upon the absorbed and emitted radiation, the orbit plane of the debris object with respect to an inertial reference frame is specified. This reference frame is centered on the Earth and has its x-axis pointing toward the sun, its z-axis aligned with the rotation axis of the Earth, and $y = z \times x$. For purposes of the model, it is assumed that the axial tilt of the Earth with respect to the ecliptic plane is 0°. The debris orbit plane is specified by the inclination of the orbit and the local-time location of the ascending node (see Appendix B). The initial position of the debris object is assumed to be the ascending node. Since the orbit of the debris object is assumed to be circular, the position of the debris in its orbital plane is easily computed. The debris position vector is then rotated into the reference frame and the energy input and loss are calculated, resulting in a temperature change (dT/dt) for the time step. The temperature is adjusted and the next step is taken. The initial temperature for the debris was arbitrarily chosen as 285 °K. Other initial temperatures were considered and found to have no effect on the conclusions.

## 5.2 PREDICTED THERMAL BEHAVIOR OF THE ANOMALOUS DEBRIS

The thermal model has been applied to several hypothetical debris pieces and orbits in order to understand how the various components of the model affect the debris temperature, and then applied to the actual debris and orbits found in this work. For the hypothetical case two droplet masses were selected for consideration: 57 grams and 1 gram. The larger (smaller) mass corresponds to a sphere with radius 2.5 cm (6.5 mm) at 285 °K and roughly cover the proposed size range for these debris. The orbits were assumed to be circular, with an inclination of 65°, and the right ascension of the ascending node was varied. The altitude was also allowed to vary between 850-1000 km The results for both spheres at an altitude of 925 km are displayed in Figure 15. Each figure shows three curves which correspond to debris with ascending nodes located at 1200 local time (i.e., local noon), 1500 LT, and 1800 LT (i.e., local dusk). Consider the 57 gm sphere in Figure 15a. When the local time of the ascending node (LTAN) is 1800 the sphere never enters eclipse and gradually warms to a temperature of ~326 °K. The small temperature fluctuation is a result of the variation in Earth-reflected sunlight over the course of an orbit As the LTAN decreases, the droplet begins to undergo eclipse and a sawtooth pattern develops in the thermal history. At LTAN=1500 the sphere's temperature varies between 302-313 °K, while at LTAN=1200 the temperature varies between 289-311 °K. Due to the symmetry of this model about the Earth-sun line, the temperature of debris in orbits with ascending nodes at other local times varies in the same fashion; therefore, this set of three orbits is representative of the temperature variation of the debris as a function of ascending node location. Note that the variation in temperature is a maximum for the orbit with LTAN=1200; this is because the sphere spends more time in eclipse in this orbit than in any of the others, allowing it to cool to lower temperatures. Note that the temperature of the 57 gm sphere never decreases below the freezing point of eutectic NaK, implying that the sphere remains in the liquid state.

The behavior of the 1 gm sphere is presented in Figure 15b. The less massive sphere undergoes larger temperature variations during its orbit, but its temperature remains well above the freezing point of eutectic NaK. The larger temperature variation is due to the fact that the energy input scales as r^2 (area) while the thermal mass scales as r^3 (volume). Therefore, dT/dt varies as r^{-1}, and is larger for smaller/less massive droplets.

The variation of the droplet temperatures as a function of altitude is presented in Table 5. The temperature of the droplets remain above 260 °K at all relevant altitudes.
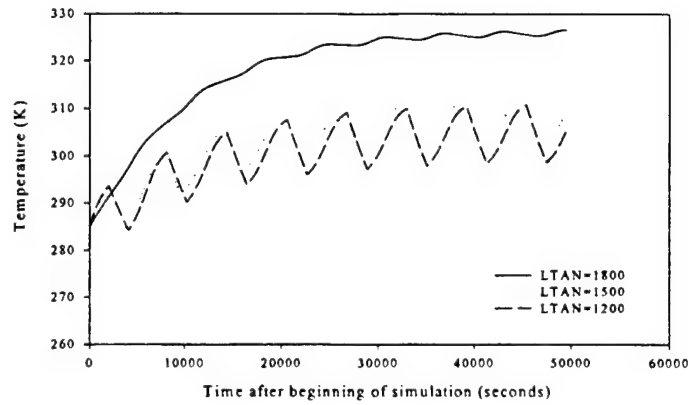
(15a)
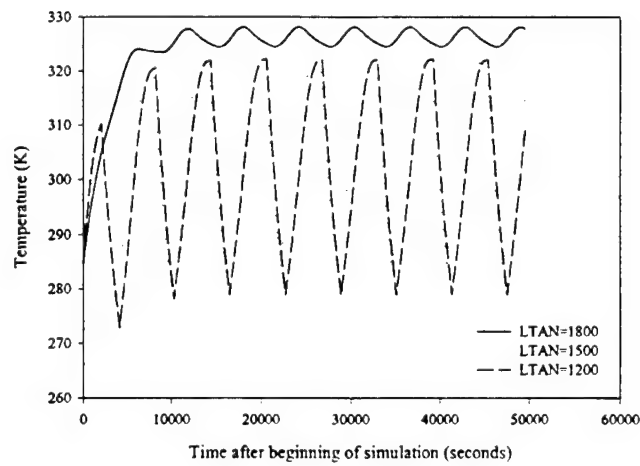
(15b)

Figure 15. Thermal modeling results for (a) 57 gm sphere at 925 km altitude, φ=65°, and local time of ascending node (LTAN) at 1200, 1500, and 1800; (b) 1 gm sphere with the same parameters.

TABLE 5

Thermal Modeling Results

Altitude (km)	LTAN	57 gm sphere Temperature (K)	1 gm sphere Temperature (K)
850	12	300-312	280-324
850	15	303-310	286-324
850	18	327-328	326-330
925	12	289-311	279-322
925	15	302-313	285-322
925	18	326	323-326
1000	12	297-309	277-320
1000	15	300-311	283-321
1000	18	323-325	323-327

In Figure 16, thermal history curves for the eleven anomalous debris orbits are presented; the orbital elements for the debris are presented in Table 6. Individual thermal histories are difficult to discern, but the envelope of the temperature variations is evident. None of the anomalous debris temperatures drop below 260 °K. Therefore it is inferred that the anomalous debris are likely to be *liquid* NaK droplets.
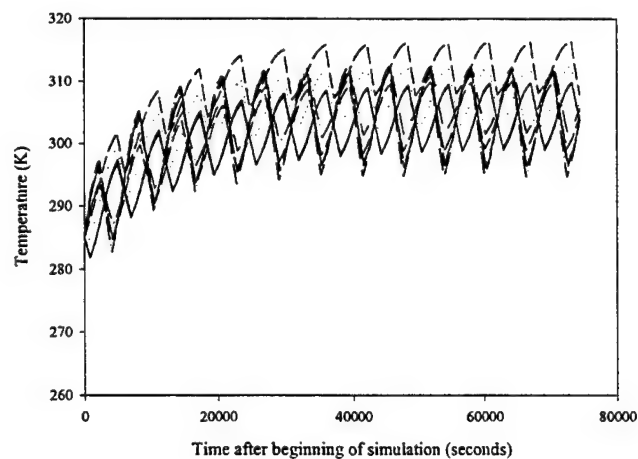

Figure 16. Compilation of the modeled thermal histories for the debris objects listed in Table 5.

31

TABLE 6

Orbital Parameters for Anomalous Debris

Object Number	Inclination	Eccentricity	Right Ascension	Semi-Major Axis (R_E)
81215	64.96°	0.004	304.38°	1.146
33562	65.04°	0.004	77.291°	1.146
33609	64.96°	0.005	203.35°	1.146
33612	64.97°	0.005	187.93°	1.146
33616	64.69°	0.006	207.65°	1.147
39969	64.69°	0.006	222.31°	1.147
39970	64.65°	0.006	207.86°	1.147
39971	64.96°	0.004	300.13°	1.146
39972	64.97°	0.005	202.81°	1.146
39973	65.05°	0.004	86.32°	1.146

This model is not a high-fidelity calculation of the debris temperature. The calculation performed here is sufficient to demonstrate whether the temperatures of the spheres lies near the freezing point of eutectic NaK; it is concluded that they do not. A discussion of the limitations of the model is useful. It was assumed that the albedo of the Earth is a globally-averaged constant with a value of 0.34. In reality, the albedo of the Earth is dependent upon the reflective nature of the surface and the amount of cloud cover. The surface albedo is in turn dependent upon the nature of the surface; water, snow, vegetation, and desert all reflect light differently. Cloud albedo is also dependent upon the type and thickness of the cloud cover[18]. Obviously, the globally-averaged albedo does not remain constant; *Peixoto and Oort* [1992] suggest that it varies between 0.26 and 0.32 annually. A second issue related to albedo is that for low-altitude objects, the debris temperature is dependent upon the average albedo of the Earth scene which is visible to it, not the albedo of the entire globe. This number can vary from ~0.25 to ~0.70 (Ref. 21). To address both of these issues, a test was run with the albedo set to 0.0 to determine how much the debris temperature decreases. For a droplet at 925 km altitude, 65° inclination and LTAN = 1200, the temperature ranges from ~289-301 °K, a 9-10° decrease. For LTAN=1800, the temperature decrease is ~3 degrees. The debris temperature does not fall below the eutectic NaK freezing point even in the absence of Earth-reflected sunlight.

The Earth's rotation axis tilt of ~23° away from the normal to the ecliptic plane was neglected. The tilt will cause a seasonal eclipsing of the debris and thus a seasonal effect in the temperature of the debris. Consider a NaK sphere with LTAN = 1800 (dusk terminator) and an orbital inclination of 65°. At the winter solstice, the Earth's axis is tipped ~23° away from the sun. This reduces the angle between the ecliptic and the orbit plane by ~23° to 42° (see Figure 17a). The sphere will then be eclipsed during a portion

of its orbit. For debris with LTAN = 0600 (dawn terminator), the debris can enter eclipse during southern hemisphere winter. This effect is simulated by reducing the orbital inclination in the model to 42°; the predicted temperature of the debris at 925 km altitude was reduced from 326 °K to the range of 302-312 °K (Figure 17b). This is still well above the freezing point of eutectic NaK.
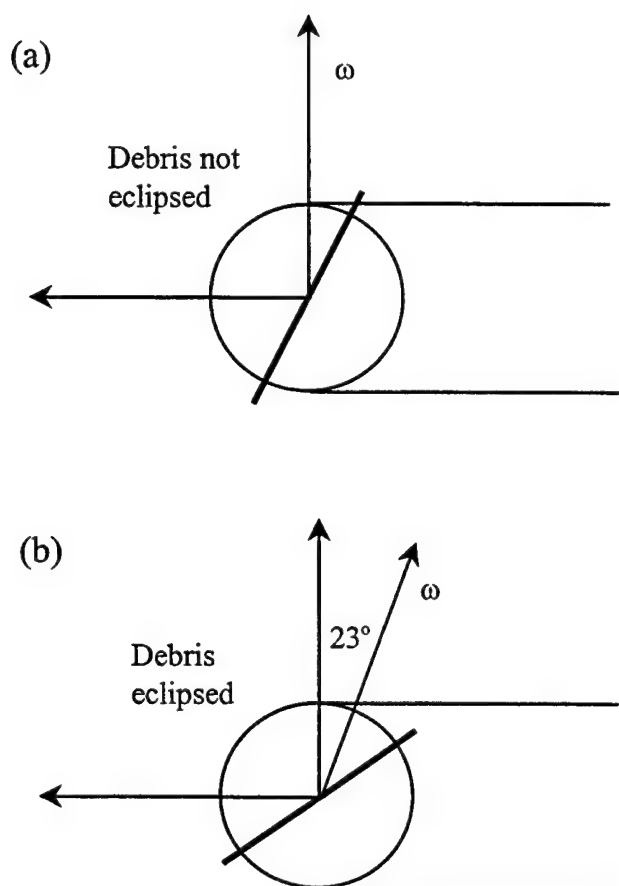
Figure 17. Cartoon depicting the seasonal eclipsing of debris with LTAN=1800: (a) debris orbit at the equinox, (b) debris orbit at northern hemisphere winter solstice.

Finally, it is noted that the computed debris temperatures depend *strongly* on absorptivity and emissivity values. If these values are inaccurate, the conclusion that the debris are liquid could be incorrect. However, based on the available literature on the subject, a reasonable estimate of the absorptivity and emissivity values for NaK has been made, and hence it is concluded that the debris are probably in the liquid state.

5.3 EFFECT OF EVAPORATION ON EVOLUTION OF THE DEBRIS ORBITS

Given that the anomalous debris are in the liquid state, the question of whether these droplets evaporate and the time scale over which evaporation occurs can have important implications for the orbital lifetime. The atmospheric drag force on the droplets depends upon the ratio of projected area to mass. Loss of mass due to evaporation would lead to a change in the area-to-mass ratio and variation of the drag force on the debris. This could allow the debris to decay into heavily used orbits.

The flux of evaporating particles can be estimated from the principles of kinetic theory. Particles in the liquid with kinetic energies greater than the work necessary to move the particle from its initial position to infinity will escape into the surrounding space. This "work function" for the liquid can also be thought of as the latent heat of evaporation referred to a single particle. A minimum "escape velocity" for the particle can be derived from $mv^2/2 = U_O$, where U_O is the latent heat of evaporation mentioned above. Then, estimation of the escaping flux is a simple matter of calculating the first moment of the liquid's velocity distribution function.

However, no value for the latent heat of evaporation for the NaK liquid was available. Also, a velocity distribution function for the droplet has to be assumed. Therefore, the assumption was made that the rate of evaporation is equal to the rate at which the vapor particles would strike the liquid if the liquid and the vapor were in equilibrium. This rate is:

$$W(kg/\sec) = \kappa A_s P \sqrt{\frac{M}{2\pi RT}} \tag{16}$$

where κ is the evaporation coefficient, A_s is the surface area of the droplet, P is the vapor pressure at temperature T, M is the molar weight of the element, and R is the universal gas constant. This is the maximum rate of evaporation (Ref. 25). No measurements of the vapor pressure of the eutectic NaK system at the low temperatures which the droplets experience on orbit were found. Therefore, an evaporation theory which applies to binary alloys was adopted. The evaporation rate is slightly modified to account for the two different components. It is expressed as:

$$W_i(kg/\sec) = \kappa_i A_s P_i^o \gamma_i(x) N_i \sqrt{\frac{M_i}{2\pi RT}} \tag{17}$$

where γ is the activity coefficient, and i refers to a specific component (Na or K in this case). The mole fractions, N_i, are expressed as:

$$N_{Na} = \frac{\left[\dfrac{(a-x)}{M_{Na}}\right]}{\left[\dfrac{(a-x)}{M_{Na}} + \dfrac{(b-y)}{M_K}\right]} \tag{18a}$$

$$N_K = \frac{\left[\dfrac{(b-y)}{M_K}\right]}{\left[\dfrac{(a-x)}{M_{Na}} + \dfrac{(b-y)}{M_K}\right]} \tag{18b}$$

Note that as time passes and more of each element evaporates from the system, the mole fractions change (as do the atomic fractions of Na and K and the activity coefficient, γ). Determination of the time scale for evaporation of the droplets required numerical solution of the following coupled differential equations:

$$\frac{dx}{dt} = W_{Na}(x,y)$$

$$\tag{19}$$

$$\frac{dy}{dt} = W_K(x,y)$$

In order to calculate evaporation rates, the vapor pressures of Na and K and the activity coefficients must be known. The vapor pressures of Na and K at low pressures and temperatures ranging from their normal melting points (371 °K for Na, 337 °K for K) to ~463 °K are given by the following relations:

$$\log P_{Na} = 8.08 - \frac{5479}{T}$$

$$\tag{20}$$

$$\log P_K = 7.56 - \frac{4587}{T}$$

where P is in torr and T is in °K. The activity coefficients are given in Table 7 (Ref. 26).

As in the last section, droplets with masses of 1 gm and 57 gm were considered. To facilitate the calculation of evaporation rates, the droplets were assumed to maintain an average temperature over an orbit, and three temperatures were considered: 300, 330, and 280 °K. These temperatures correspond to debris in orbits which are eclipsed, orbits which are not eclipsed, and an arbitrary low temperature, respectively.

For eutectic NaK, the droplets are 77.8% K by mass, therefore the 57 gm (1 gm) droplet initially contains 44.346 gm (0.778 gm) of K and 12.654 gm (0.222 gm) of Na. The initial atomic fraction of Na in the droplets was 0.3267 (32.67% of the atoms in the droplets were Na atoms); this was used to interpolate the initial activity coefficients for

the systems. The initial vapor pressures were calculated using equation (20), and it is assumed that the vapor pressures do not change as the elements evaporate. It is further assumed that the composition of the droplets remains uniform. These two important assumptions will be discussed below. Note also that the vapor pressure formulae are being applied at temperatures below which they are deemed applicable because the NaK system is still liquid at these temperatures. Given these initial conditions, equations (19) are integrated using a timestep of 86400 seconds. The initial evaporation rates are so small (4.03348×10^{-12} kg/m²-s for Na; 4.21491×10^{-9} kg/m²-s for K), that the relatively large timestep is acceptable. It should be noted that the simulation is stopped if a phase transition is brought on by the changing composition of the droplet.

Figure 18 presents the results of the evaporation simulation for the 57 gm droplet at 300 °K. The simulation covered ~79 years. The mass loss from the droplet in total and for the individual components is shown in the top panel. The Na component evaporates very little over the course of the simulation. The K component evaporates at a relatively rapid pace, and after ~79 years the composition of the drop has changed sufficiently to raise the melting point above 300 °K (*i.e.,* solidification begins). The second panel shows the change in the radius of the droplet; the radius decreases by ~0.75 cm during the simulation. The third panel shows the evaporation rates for each component of the alloy. The rates slow as the elements evaporate from the system and the mole fractions decrease. The effect of the phase transition on the system is discussed below.
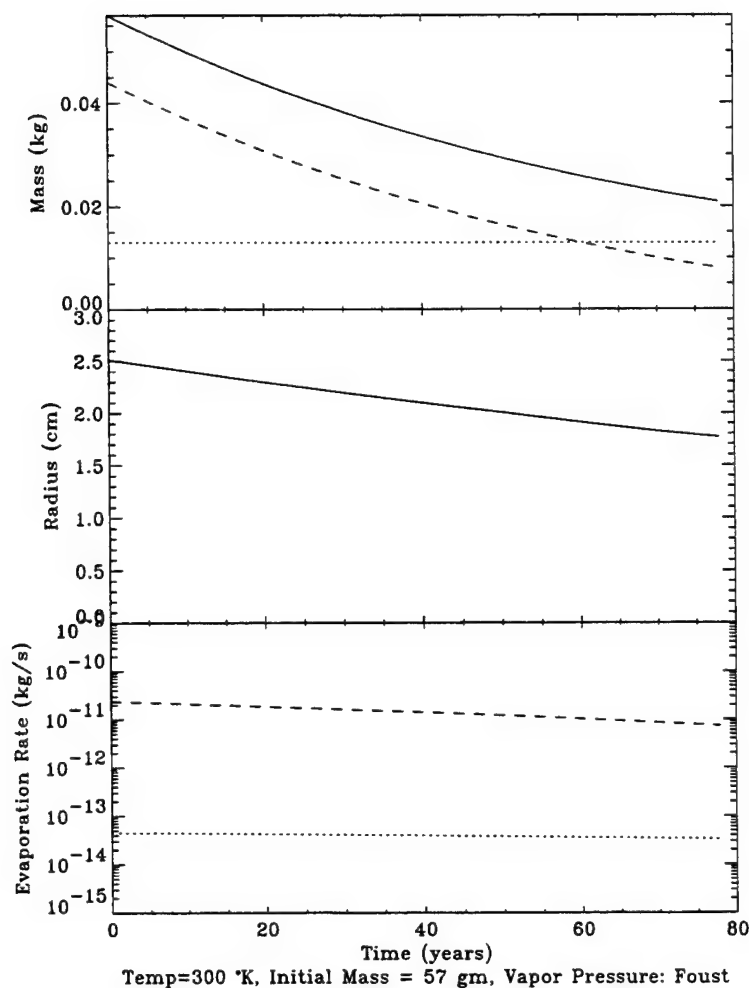
Figure 18. Results of the evaporation modeling for the 57 gm droplet with a temperature of 300 °K. In each panel, the dashed line represents the potassium component, the dotted line represents the sodium component, and the solid line represents the sum of the two components. The top panel displays the mass history, the middle panel shows the change in radius of the drop with time, and the bottom panel displays the evaporation rates.

Figure 19 shows the results for the 57 gm droplet at a temperature of 330 °K. In this case, the potassium evaporated rapidly and the droplet began solidifying after ~4 years. This rapid evaporation can be explained by examination of equations (19); a 30° increase in temperature increases the initial potassium vapor pressure from 2.475×10^{-6} Pa to 6.075×10^{-5} Pa, a factor of ~24 increase. The evaporation rate is directly proportional to the vapor pressure; therefore, it also increases by a factor of ~24. This demonstrates that the evaporation rate is extremely sensitive to the value of the vapor pressure.

Figure 19. Evaporation results for the 57 gm droplet at 330 °K in the same format as Figure 7.

Figure 20 shows the results for the 1 gm droplet at a temperature of 300 °K. Sufficient potassium evaporates from this system in ~20 years for solidification to begin, slightly faster than for the larger droplet. Considering that the evaporation rate is lower (third panel of Figure 20), this result is counterintuitive. However, for a given period of time, the mass loss per unit mass ($\Delta m/m$) is larger for smaller droplets ($\Delta m/m \sim r^{-1}$), causing the smaller droplets evaporate more quickly. The radius of the droplet decreases from 6.5 mm to ~ 4.5 mm over the course of the simulation.
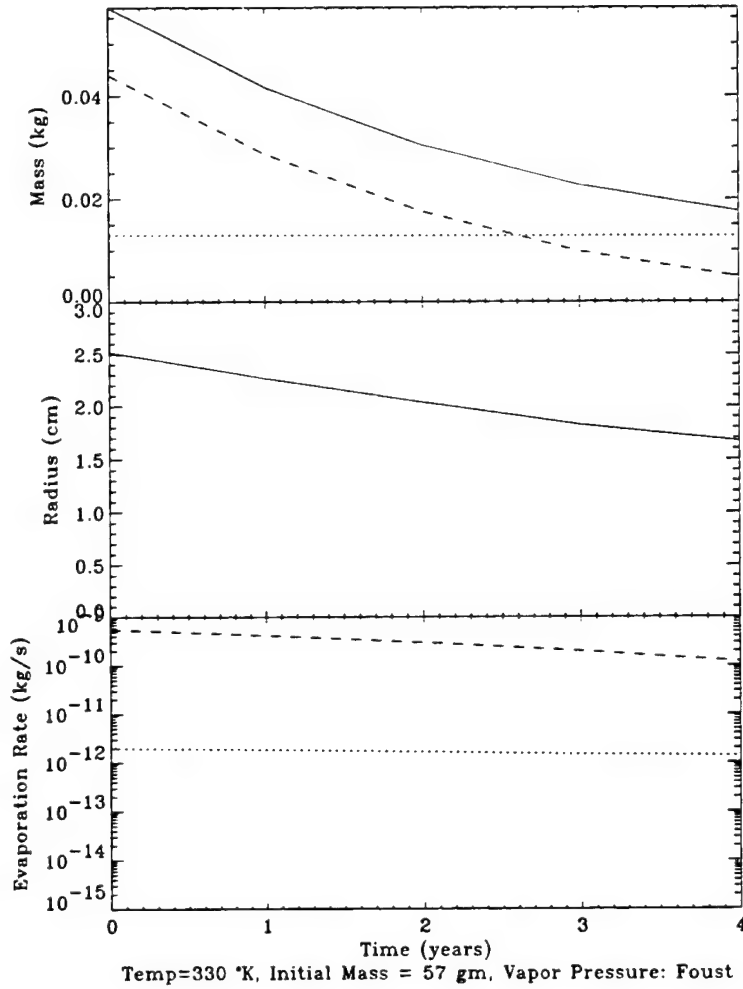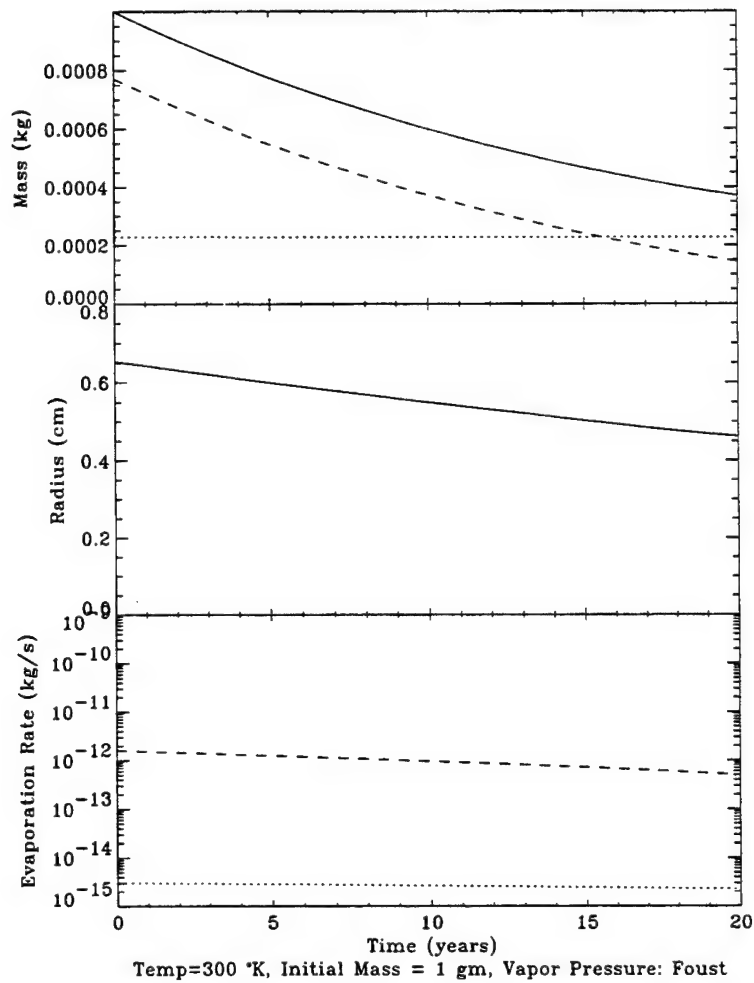
Figure 20. Evaporation results for the 1 gm droplet at 300 °K in the same format as Figure 7.

Figure 21 shows the results for the 1 gm droplet at 330 °K. Sufficient potassium evaporates from the system in ~1 year to induce solidification. The radius of the droplet decreased to ~4 mm. Table 8 presents the results for all of the simulations.
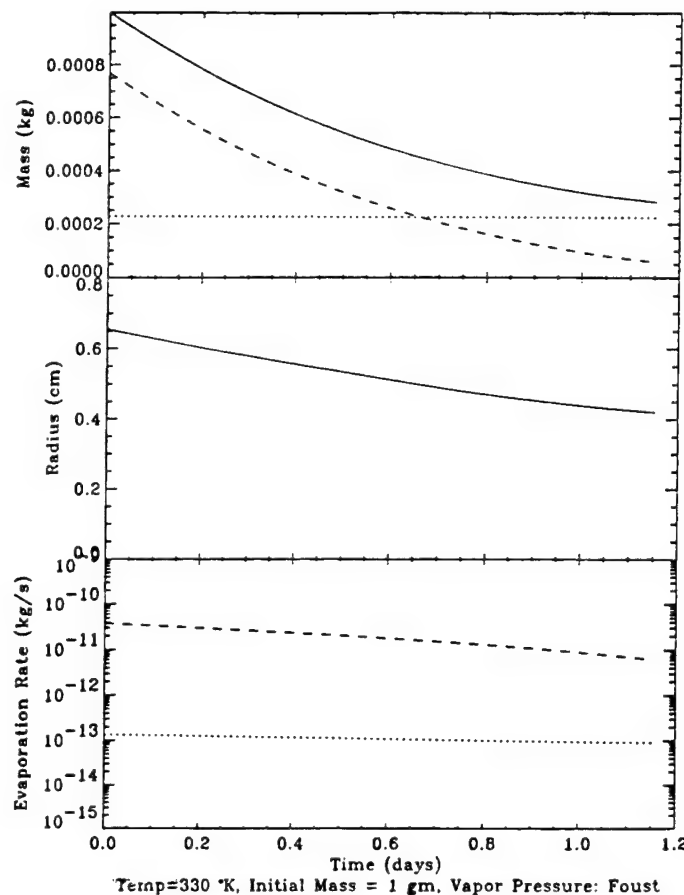
39

Figure 21. Evaporation results for the 1 gm droplet at 330 °K in the same format as Figure 7.

Table 8 shows that the NaK droplets always go through a phase transition which is induced by the change in composition as they evaporate. In Figure 22, the phase diagram for NaK is presented. The eutectic mixture (the starting point in the simulations) is denoted. The melting point for the various mixtures is marked by the top line in the plot (liquidus). As the droplet evaporates at constant temperature, the fraction of K decreases relatively rapidly. Eventually, the melting point rises above the temperature maintained in the simulation and solidification of the liquid begins. For the temperature range considered in this note, the NaK changes to a mixture of liquid and solid when the liquidus is crossed. The composition of the liquid (solid) is given by the composition at which the constant temperature line intersects the liquidus (solidus). For example, at 300 °K, when the K mass fraction decreases to ~40%, the liquid has a composition of ~40 % K and ~60 % Na by mass/weight, while the forming solid has a composition of ~6 % K and ~94 % Na by mass/weight. *The relative compositions of this liquid/solid mixture will not change unless the temperature is changed*; for additional evaporation of the K to occur, the temperature must be increased (Ref. 27,28). The simulation was stopped at the phase transition because very little is known about how the droplet solidifies or the differences in evaporation from the liquid and solid alloys. Examination of Tables 8 and 9 show that once solidification begins, anywhere from 15% - 50% of the droplet's original mass still remains. Therefore, complete evaporation of the droplets could take much longer than the time scales presented above.

40

TABLE 7

Activity Coefficients for Liquid NaK at 298.15 °K

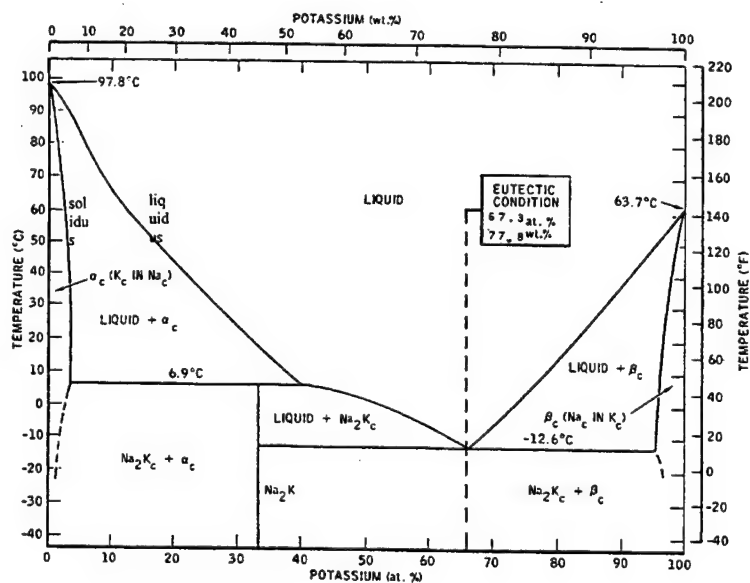| Atomic Fraction Na	γ_{Na} (± 0.06)	γ_K (± 0.06)
0.0	3.00	1.00
0.1	2.43	1.01
0.2	2.02	1.05
0.3	1.71	1.11
0.4	1.49	1.19
0.5	1.29	1.29
0.6	1.19	1.49
0.7	1.11	1.71
0.8	1.05	2.02
0.9	1.01	2.43
1.0	1.00	3.00

Figure 22. NaK phase equilibrium diagram. Phase is displayed as a function of temperature and percentage of potassium in the mixture. Adapted from Ref. 19.

TABLE 8

Simulation Results

Initial/Final Mass (gm)	Temperature (K)	Initial/Final Radius (cm)	Phase Transition (years)
57.0/28.36	280.0	2.507/1.975	634.26
57.0/20.88	300.0	2.511/1.767	78.10
57.0/16.05	330.0	2.518/1.615	4.466
1.0/0.497	280.0	0.652/0.514	164.36
1.0/0.366	300.0	0.653/0.460	20.24
1.0/0.281	330.0	0.655/0.420	1.15

It was noted earlier that the evaporation rates are very sensitive to the value of the vapor pressure(s); therefore an assessment of the accuracy of the vapor pressure values given by equations (20) is desirable. This is difficult because of the extrapolation of vapor pressure formulae for liquid Na and K down to temperatures below the freezing points of the individual elements. However, since the elements remain in the liquid state while in solution, and there is no direct measurement of the evaporation rate for NaK, this appears to be the only appropriate course of action. Crude estimates of the uncertainty in the vapor pressure values can be made by comparing extrapolations of the vapor pressure values derived by various researchers (Ref. 29). These comparisons are presented in Figures 23 (Na) and 24 (K). At 300 °K, the sodium vapor pressure agrees to within 1-2 orders of magnitude, with the value quoted in equation (20) being among the higher values. The potassium vapor pressure values agree to within an order of magnitude at 300 °K, with the value quoted by equation (20) being the lowest value. Thus, the original calculation may prove to be a lower limit on the evaporation lifetimes. However, it was chosen not to calculate evaporation lifetimes using the higher potassium vapor pressures for reasons described below.
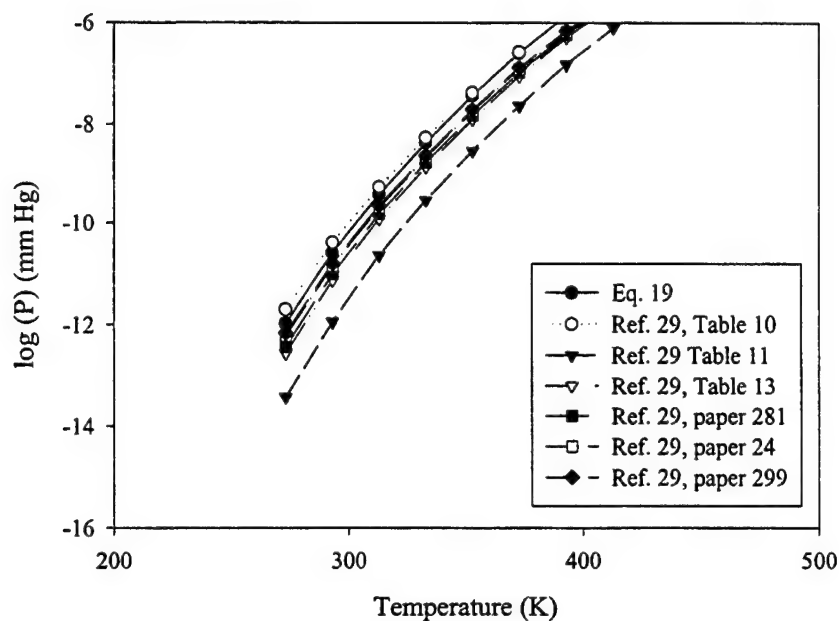
Figure 23. Comparison of sodium vapor pressure values extrapolated from the results of various researchers. Equation (20) is represented by the solid line with filled circles.
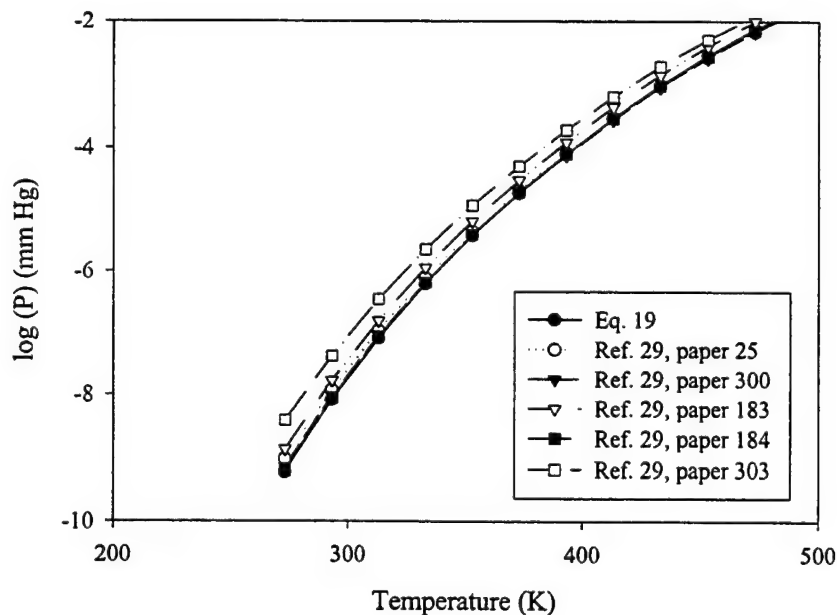

Figure 24. Comparison of potassium vapor pressure values extrapolated from the results of various researchers. Equation (20) is represented by the solid line with filled circles.

Two additional assumptions used in this model may significantly affect the calculated evaporation rates. The first assumption is that of a constant vapor pressure value in equilibrium with the droplet. For potassium, the equilibrium vapor pressure at all temperatures considered in this note is significantly larger than the ambient atmospheric pressure at the altitude of the debris, $P_{atm} \sim 10^{-8}$ Pa at 925 km (Ref. 30). It seems unlikely that the potassium vapor pressure around the droplet would attain levels ~20-6000 times that of the neutral atmosphere; the pressure gradient force would cause the potassium atoms to diffuse away from the droplet. Except at 330 °K, sodium vapor pressures remain well below atmospheric pressure. If we assume that the potassium atoms diffuse away from the droplet, the evaporation of the droplets would be slowed. To estimate the difference in evaporation rates, a series of model runs was conducted in which vapor pressures above the ambient atmospheric pressure were reduced to 10^{-8} Pa to simulate the outflow induced by the pressure gradient. Note that the sodium vapor pressures at the lower temperatures were *not* increased to remove the pressure gradient, as this would imply a second source of sodium atoms; however, at 330 °K, the sodium vapor pressure was decreased to 10^{-8} Pa. The results are presented in Table 9 and should be considered crude estimates, perhaps correct only in order of magnitude.

The second assumption, uniform composition of the droplet, implies that there is a process on orbit which continually mixes the droplet as the components evaporate. In the event that there is no mixing, only the potassium near the surface of the droplet would evaporate quickly. After this potassium evaporates, the droplet might be surrounded by a thin sodium "shell" which would evaporate at a much slower rate. This effect would also slow the evaporation of the droplets, but the effect may be minimal since the droplets are mostly potassium in the early stages of evaporation.

For droplets in certain orbits, the temperature varies as the droplet passes through sunlight and shadow; we assumed that the droplets maintained a constant temperature for computational ease. The preceding discussion has shown that the evaporation rate of the droplets is sensitive to their temperature. The effect on the evaporation rate of allowing the temperature of the droplets to vary as they evaporate was estimated by calculating the amount of material that evaporated from the droplets over the course of one orbit. In one case the temperature was allowed to vary and in the other, the temperature was held fixed at the average temperature over the orbital cycle (~303 °K for both droplets). It was found that for the 57 gm droplet, only 5.32×10^{-10} kg of evaporated when the temperature varied in a realistic fashion during the orbit, whereas 4.64×10^{-8} kg evaporated when the temperature was held constant. The 1 gm droplet behaved in the opposite manner; 9.86×10^{-11} kg evaporated when its temperature was allowed to vary compared with 3.16×10^{-11} kg when the temperature was held constant. The reason for this is that the temperature variation for the smaller droplet is larger over the course of an orbit, as shown earlier. It reaches higher temperatures than a 57 gm droplet in the same orbit, and evaporates more quickly.

The simulation was stopped when the droplets began to solidify due to a lack of information concerning the evaporation of mixed liquid/solid state. Evaporation of a solid (sublimation) at constant temperature requires an amount of heat (per mole of substance) equivalent to the sum of the latent heats of fusion and vaporization at that temperature. Evaporation of a liquid at the same temperature requires an amount of heat (per mole)

equivalent to the latent heat of vaporization at that temperature. A solid is expected to evaporate at a slower rate since the amount of energy required to liberate atoms is larger. Given the correct vapor pressures, the evaporation lifetimes could be computed using the same methods employed in this note. However, there are no known measurements of the vapor pressures for solid sodium and potassium.

The calculated evaporation lifetime is compared with the time scale for decay of the debris into the atmosphere by estimating the length of time these droplets will spend on orbit using *King-Hele* [1987] (Ref. 31, Figure 12-19). These lifetimes assume a ballistic coefficient, C_D, of 2.2 for the spheres, an atmospheric model representing an average amount of solar activity, and the initial area-to-mass ratios used in this paper. The lifetime estimates are good only to no better than ~20% and may be good to only a factor of ~two. They are presented in Table 10. Comparison of these lifetimes with the timescales presented in Table 9 suggests that it will take much longer for the droplets to evaporate significantly than it will for their orbits to decay. Previous work[2] indicates that 1 cm diameter NaK spheres at ~273 °K (m=0.46 gm) and 950 km altitude would decrease in diameter due to evaporation at a linear rate over "hundreds of years," but would re-enter the atmosphere in ~80 years. This orbital lifetime is in approximate agreement with the lifetime estimate made here for a 1 gm droplet. Russian work quoted in ref. 2 indicates that 1 cm spheres at a temperature of 293 °K would evaporate to 0.7 cm in ~100 years and is apparently consistent with the NASA calculations. These results are roughly consistent with the results presented in Table 4 derived using the maximum evaporation rates. It does not appear that any previous work has allowed for phase transitions to occur in the droplet.

TABLE 9

Simulation Results for Equalized Pressures

Initial/Final Mass (gm)	Temperature (K)	Initial/Final Radius (cm)	Phase Transition (years)
57.0/26.54	280.0	2.507/1.933	13,354.12
57.0/18.05	300.0	2.511/1.724	12,255.03
57.0/43.79	330.0	2.518/2.333	352.55
1.0/0.465	280.0	0.652/0.503	3460.61
1.0/0.317	300.0	0.653/0.448	3175.79
1.0/0.166	330.0	0.655/0.365	4610.94

TABLE 10

Approximate Orbital Lifetimes of NaK Droplets

Altitude (km)	Lifetime (m = 57 gm) (yrs)	Lifetime (m = 1 gm) (yrs)
850	172.8	45.2
925	288.0	75.3
1000	576.0	150.6

5.4 CONCLUSIONS OF THEORETICAL ANALYSIS

Based on a simple thermal model, it was found that spherical debris composed of eutectic NaK which lie in circular orbits in the altitude range of 850-1000 km are always in a liquid state. This conclusion is dependent upon the veracity of the estimate for the optical properties (α and ε) of eutectic NaK.

Given that the debris are in the liquid state, the timescale for evaporation of NaK was compared with the orbital lifetime. It seems likely that the evaporation lifetimes of these droplets range from at least ~3000 - 4000 years for the 1 gm (6.5 mm radius) droplets to at least 12,000 - 13,000 years for the 57 gm (2.5 cm radius) droplets. In this case, the lifetime on-orbit would be controlled by orbital decay and not by evaporation. However, there is significant uncertainty in these results and measurement of the evaporation rate of NaK may prove useful.

6. SUMMARY

The project has demonstrated a powerful capability for remote sensing and characterization of orbital debris (remote chemistry!) using ground-based radar and optical systems. A small sample from a particularly profuse debris field has been characterized with the following results:

1. The nature of the debris is consistent with leaked NaK fluid but remote sensing done to date cannot prove this unambiguously.
2. The debris cluster in several orbit planes with many pieces of various sizes in each plane. Both of these features are consistent with leaking liquid from the cooling system of the nuclear power source of an old Soviet satellite system.
3. No recent leak has been detected. Further the last such satellite was launched in 1989. These facts would seem to indicate that the leaks occurred soon after the nuclear power sources were put into their rest orbits as inferred.
4. All the debris detected and tracked were spherical in shape with radii < 2.8 cm. The spherical shape is again consistent with a leaking liquid.
5. The estimated density of the sample set is ~1 gm/cc which is consistent with a eutectic NaK mixture.
6. The debris are highly reflective and exhibit characteristics of specular metallic spheres - again consistent with droplets of NaK.
7. If the debris are indeed NaK and if, as indicated by the Russian manufacturers, it is an eutectic mixture, then the droplets are expected to be in liquid form due to heating by the sun and the earth.
8. If the debris are droplets of NaK, the rate of evaporation is so low that their evaporation lifetimes can exceed 10000 years. Therefore, we expect the lifetime of the debris on orbit to be primarily limited by atmospheric drag and not evaporation.

7. REFERENCES

1. E.G.Sansbery *et al*: "Haystack Radar Measurements of the Orbital Debris Environment," JSC-26655, NASA/JSC Space & Life Sciences Directorate, May 20, 1994.

2. E.G.Sansbery *et al*: "Haystack Radar Measurements of the Orbital Debris Environment : 1990-1994," JSC-27436, NASA/JSC Space & Life Sciences Directorate, April 20, 1996

3. E.G.Stansbery *et al.*, Orbital Debris Studies Using the Haystack Radar, paper presented at the 1995 Space Surveillance Workshop, MIT Lincoln Laboratory, 29 March 1995.

4. Webpage of Russian Institute of Physics and Power Engineering, http://www.rssi.ru/ippe/general/spacer.html.

5. Pearce, E. C., M. S. Blythe, D. M. Gibson, and P. J. Trujillo, Space Debris Measurements: Phase One Final Report, presented at the 1994 Space Surveillance Workshop, M.I.T. Lincoln Laboratory, Lexington, MA, March 1994.

6. Ray LeClair *et al* : Improvements in TRADEX Debris Capabilities, presented at the 1996 Space Surveillance Workshop, M.I.T. Lincoln Laboratory, Lexington, MA, March 1996.

7. Sridharan, R. Characteristics of Debris and Implications for Detection and Tracking, AAS 96-117, presented at the AAS/AIAA Space Flight Mechanics Meeting, Austin, TX, 12-15 February, 1996.

8. Ruck, G. T. (ed.), *Radar Cross-Section Handbook*, Plenum Press, New York, 1970.

9. Hedin, A. E., A Revised Thermospheric Model Based on Mass Spectrometer and Incoherent Scatter Data: MSIS83, *J. Geophys. Res. A*, **88**, 10170, 1983.

10. Gaposchkin, E. M., and A. J. Coster, Analysis of Satellite Drag, *The Lincoln Laboratory Journal*, **1**, 203, 1988.

11. Gaposchkin, E. M., and A. J. Coster, Evaluation of Recent Atmospheric Density Models, *Adv. Space Res.*, **6**, 157, 1986.

12. Miller, R. R., *Liquid Metals Handbook, Sodium (NaK) Supplement*, C. B. Jackson (ed.), Atomic Energy Commission and the Dept. of the Navy, 1955.

13. Allen, C. W., *Astrophysical Quantities*, The Athlone Press, London, 1983.

14. Williams, J. G., and G. A. McCue, *Planet. Space Sci., 14*, pp. 844, 1966.

15. Hecht, E., *Optics*, Addison-Wesley Publishing Co., Reading, MA, 1988.

16. Cunningham, F. G., Earth Reflected Solar Radiation Input to Spherical Satellites, *ARS Journal*, **32**,1033, 1962.

17. W. L. Wolfe, and G. J. Zissis, *The Infrared Handbook*, Office of Naval Research, Washington, D. C., 1978.

18. Peixoto, J. P., and A. H. Oort, *Physics of Climate*, AIP Press, New York, 1992.

19. Foust, O. J. (ed.), *Sodium NaK Engineering Handbook Vol.* 1, Gordon and Breach, New York, 1972.

20. Meshcheryakov, S. A., Physical Characteristics of Alkaline Metals and Behavior of Liquid Metal Coolant Droplets in Near-Earth Orbits, paper presented at the Second European Conference on Orbital Debris, Darmstadt, Germany, March 1997.

21. Morgan, R., The Optical Constants of Sodium-Potassium Alloys, *Phys. Rev.*, **20**, pp. 203, 1922.

22. Jackson, J. D., D. K. W. Tong, P. G. Barnett, and P. Gentry, Measurement of liquid sodium emissivity, *Nucl. Energy*, **26**, pp. 387, 1987.

23. Hattori, N., H. Takasu, and T. Iguchi, Emissivity of liquid sodium, *Heat Transfer, Jap. Res.*, **13**, pp. 30, 1984.

24. Kamiuto, K., Radiative properties of liquid potassium, *J. Nucl. Sci. and Tech.*, 23, pp. 372, 1986.

25. R. Ohno, Kinetics of Evaporation of Various Elements from Liquid Iron Alloys under Vacuum, in *Liquid Metals*, S. Z. Beer (ed.), Marcel Dekker, Inc, New York, 1972.

26. R. R. Hultgren *et al*, *Selected Values of Thermodynamic Properties of Metals and Alloys*, Wiley, New York, 1963.

27. P. Gordon, *Principles of Phase Diagrams in Materials Systems*, McGraw-Hill Book Company, New York, 1968.

28. A. G. Guy and J. J. Hren, *Elements of Physical Metallurgy*, Addison-Wesley, Reading, Ma, 1974.

29. A. N. Nesmeyanov, *Vapor Pressure of the Chemical Elements*, Elsevier Publishing Company, New York, 1963.

30. Jursa, A (ed.), *Handbook of Geophysics and the Space Environment*, Air Force Geophysics Laboratory, Hanscom AFB, MA 1985.

31. D. King-Hele, *Satellite Orbits in an Atmosphere: Theory and Applications*, Blackie and Son, Ltd., London, 1987

REPORT DOCUMENTATION PAGE

1. AGENCY USE ONLY (*Leave blank*)	2. REPORT DATE 18 December 1998	3. REPORT TYPE AND DATES COVERED Technical Report

4. TITLE AND SUBTITLE

A Case Study of Debris Characterization by Remote Sensing

5. FUNDING NUMBERS

C — F19628-95-C-0002

6. AUTHOR(S)

R. Sridharan, W.I. Beavers, E.M. Gaposhkin, R.L. Lambour, and J.E. Kansky

7. PERFORMING ORGANIZATION NAME(S) AND ADDRESS(ES)

Lincoln Laboratory, MIT
244 Wood Street
Lexington, MA 02420-9108

8. PERFORMING ORGANIZATION REPORT NUMBER

TR-1045

9. SPONSORING/MONITORING AGENCY NAME(S) AND ADDRESS(ES)

NASA/Johnson Space Center
2101 NASA Road 1
Houston, TX 77058

10. SPONSORING/MONITORING AGENCY REPORT NUMBER

ESC-TR-97-098

11. SUPPLEMENTARY NOTES

None

12a. DISTRIBUTION/AVAILABILITY STATEMENT

Approved for public release; distribution is unlimited.

12b. DISTRIBUTION CODE

13. ABSTRACT (*Maximum 200 words*)

Analysis of orbital debris data has revealed a band of anomalously high debris concentration between 800 Km, and 1000 Km, altitudes. Detective work by NASA has shown the likely origin to be leaking coolant fluid from nuclear power sources that powered a now defunct Soviet space-based series of ocean surveillance satellites. A project has been in progress at MIT Lincoln Laboratory to detect, track and characterize a small sample of the anomalous debris. The primary sensors used for the purpose are the Haystack radar, the Millstone hill radar, TRADEX and the Firepond optical observatory. The major question addressed was — can we infer the composition of the material the droplets are made of? The techniques being used to detect, track and characterize the sample set will be described in this report. Results of the characterization analysis will also be presented.

14. SUBJECT TERMS

15. NUMBER OF PAGES 64

16. PRICE CODE

17. SECURITY CLASSIFICATION OF REPORT Unclassified	18. SECURITY CLASSIFICATION OF THIS PAGE Same as Report	19. SECURITY CLASSIFICATION OF ABSTRACT Same as Report	20. LIMITATION OF ABSTRACT Same as Report